Buried Underwater Munitions and Clutter Discrimination
FINAL REPORT

SERDP Project MR-1717

Dr. Jesse McNinch

U.S. Army Engineer Research and Development Center (ERDC)

John Dubberley, Dr. William Sanders

Naval Research Laboratory

Report Documentation Page

Form Approved
OMB No. 0704-0188

1. REPORT DATE	2. REPORT TYPE	3. DATES COVERED
OCT 2010		**00-00-2010 to 00-00-2010**

4. TITLE AND SUBTITLE	5a. CONTRACT NUMBER
Buried Underwater Munitions and Clutter Discrimination	5b. GRANT NUMBER
	5c. PROGRAM ELEMENT NUMBER
6. AUTHOR(S)	5d. PROJECT NUMBER
	5e. TASK NUMBER
	5f. WORK UNIT NUMBER
7. PERFORMING ORGANIZATION NAME(S) AND ADDRESS(ES) **U.S. Army Engineer Research and Development Center (ERDC),3909 Halls Ferry Road,Vicksburg,MS,39180-6199**	8. PERFORMING ORGANIZATION REPORT NUMBER
9. SPONSORING/MONITORING AGENCY NAME(S) AND ADDRESS(ES)	10. SPONSOR/MONITOR'S ACRONYM(S)
	11. SPONSOR/MONITOR'S REPORT NUMBER(S)

12. DISTRIBUTION/AVAILABILITY STATEMENT
Approved for public release; distribution unlimited

13. SUPPLEMENTARY NOTES

14. ABSTRACT

Background - Low-frequency Synthetic Aperture Sonar (LF-SAS) in tandem with magnetic sensing techniques have successfully demonstrated the ability to detect buried underwater munitions; however, these sensors also detect an inordinate amount of buried clutter. Processing techniques are needed to discriminate buried munitions from clutter. SERDP SON Number MMSON-10-02 stated that ?clutter represent potentially significant sources of false alarms making detection and remediation of underwater munitions difficult and costly.? Objective - The long-term objective of this joint research effort between the U.S. Army Engineering Research and Development Center (ERDC) and the Naval Research Laboratory (NRL) is to develop automated methods to discriminate buried underwater munitions from buried clutter by extending NRL?s patented 2-D clutter classification techniques to the 3-D sub-bottom environment. These new techniques include the first phase of a clutter classification model that uses characteristics of buried munitions and clutter derived from modeled acoustic and magnetic signatures. Validation of the discrimination methods will be performed in a controlled environment at an environmentally representative field site in follow-on research. Technical Approach - The prior art of 2-D seafloor clutter discrimination detects mine-like objects in acoustic imagery and classifies them as mines or clutter based upon object dimensions, acoustic shadows, brightness and shape. To achieve the objectives, distinguishable characteristics between munitions and clutter were discovered through modeling and controlled experiments. The proposed 3-D Munitions and Clutter Classifier (MACC), which will be finalized in a follow-on study, will rely on NRL?s automated techniques, including derived bottom clutter, roughness, 2-D side scan detection, 3-D sub-bottom detection, and magnetic detection. Bayesian inference will be used to fuse the various detection sensors. The detections will be passed to a Support Vector Machine (SVM) classifier, which will examine feature vectors in - or derived from - the detection sensors. The classifier will separate unexploded ordnance (UXO) from UXO-like targets. UXO signatures will be obtained and MACC will be calibrated at the Army?s underwater test facility at Duck, North Carolina. Parametric sonar and magnetic surveys will be conducted over inert munitions and clutter placed in different sediments types and at different sub-bottom depths to test the methods. Results - For this SEED project, previously collected data was examined to help select test sites. A survey was conducted in Duck, North Carolina, and three sites were selected to reflect the desired environmental and operational variability. Side scan Automated Target

15. SUBJECT TERMS

16. SECURITY CLASSIFICATION OF:			17. LIMITATION OF ABSTRACT	18. NUMBER OF PAGES	19a. NAME OF RESPONSIBLE PERSON
a. REPORT	b. ABSTRACT	c. THIS PAGE			
unclassified	**unclassified**	**unclassified**	**Same as Report (SAR)**	**48**	

This document is approved for public release.

This report was prepared under contract to the Department of Defense Strategic Environmental Research and Development Program (SERDP). The publication of this report does not indicate endorsement by the Department of Defense, nor should the contents be construed as reflecting the official policy or position of the Department of Defense. Reference herein to any specific commercial product, process, or service by trade name, trademark, manufacturer, or otherwise, does not necessarily constitute or imply its endorsement, recommendation, or favoring by the Department of Defense.

Table of Contents

Figures and Tables

Figures

Tables

Abstract

Background - Low-frequency Synthetic Aperture Sonar (LF-SAS) in tandem with magnetic sensing techniques have successfully demonstrated the ability to detect buried underwater munitions; however, these sensors also detect an inordinate amount of buried clutter. Processing techniques are needed to discriminate buried munitions from clutter. SERDP SON Number MMSON-10-02 stated that "clutter represent potentially significant sources of false alarms making detection and remediation of underwater munitions difficult and costly."

Objective - The long-term objective of this joint research effort between the U.S. Army Engineering Research and Development Center (ERDC) and the Naval Research Laboratory (NRL) is to develop automated methods to discriminate buried underwater munitions from buried clutter by extending NRL's patented 2-D clutter classification techniques to the 3-D sub-bottom environment. These new techniques include the first phase of a clutter classification model that uses characteristics of buried munitions and clutter derived from modeled acoustic and magnetic signatures. Validation of the discrimination methods will be performed in a controlled environment at an environmentally representative field site in follow-on research.

Technical Approach - The prior art of 2-D seafloor clutter discrimination detects mine-like objects in acoustic imagery and classifies them as mines or clutter based upon object dimensions, acoustic shadows, brightness and shape. To achieve the objectives, distinguishable characteristics between munitions and clutter were discovered through modeling and controlled experiments. The proposed 3-D Munitions and Clutter Classifier (MACC), which will be finalized in a follow-on study, will rely on NRL's automated techniques, including derived bottom clutter, roughness, 2-D side scan detection, 3-D sub-bottom detection, and magnetic detection. Bayesian inference will be used to fuse the various detection sensors. The detections will be passed to a Support Vector Machine (SVM) classifier, which will examine feature vectors in - or derived from - the detection sensors. The classifier will separate unexploded ordnance (UXO) from UXO-like targets. UXO signatures will be obtained and MACC will be calibrated at the Army's underwater test facility at Duck, North Carolina. Parametric sonar and magnetic surveys will be conducted over inert munitions and clutter placed in different sediments types and at different sub-bottom depths to test the methods.

Results - For this SEED project, previously collected data was examined to help select test sites. A survey was conducted in Duck, North Carolina, and three sites were selected to reflect the desired environmental and operational variability. Side scan Automated Target Recognition (ATR) algorithms were improved and applied to the problem, as were volumetric ATRs. Magnetic ATRs were discussed for future implementation. A preliminary design and revised technical approach to MACC was developed using Bayesian Inference to determine when the various sensors would collectively come to a detect decision, and using SVM classifiers to classify the detects. This two-stage process is expected to significantly lower the incidence of false alarms.

Benefits - The improved discrimination techniques developed through this effort will significantly reduce time, effort, and thus operational costs associated with typical underwater UXO remediation efforts. By more accurately identifying clutter, the false detection rate can be reduced allowing for more efficient recovery of munitions. New sub-bottom sensors are capable of improved detection of UXO; however, they also detect increased amounts of clutter, driving the need for improved clutter

discrimination techniques. This new technology will benefit both Army's munitions remediation efforts and Navy's mine-hunting operations.

Objective

The long-term objective of this joint research effort between the ERDC and NRL is to develop automated methods to discriminate buried underwater munitions from buried clutter in the 3-D sub-bottom environment. This seed project centered on showing the practicality of an at-sea test range, bringing together the various detectors into the NRL Environmental Post Mission Analysis (EPMA) software framework, developing a detection scheme for 3-D acoustic imagery, and designing a first phase clutter classifier that uses characteristics of buried munitions and clutter derived from modeled acoustic and magnetic signatures. Validation of the discrimination methods will be performed in a controlled environment at an environmentally representative field site during a follow-on study.

Background

This project addresses SERDP Munitions Management Statement of Need Number MMSON-10-02: Improvements in the Detection and Remediation of Underwater Military Munitions. The researchers have developed techniques to discriminate buried clutter from munitions through exploitation of unique clutter/target signatures and characteristics detected from advanced acoustic and magnetic sensors. This work addresses a high priority need to significantly improve the Department of Defense (DoD) ability to characterize and remediate small (20 mm) to large (2000 lb) munitions existing at numerous underwater sites in depths up to 120 feet.

In July 2007, SERDP & ESTCP sponsored a workshop to identify the research, development, test, and evaluation (RDT&E) needs to survey underwater UXO contaminated sites. Based on this workshop, and detailed in the Final Report *SERDP and ESTCP Workshop On Technology Needs for the Characterization, Management, and Remediation of Military Munitions in Underwater Environments* (1), several needs were identified, with an emphasis on the need for improved methods to discriminate between UXOs and clutter as a "Critical Priority".

As a result of former military training, weapons testing, or inadvertent unloading, UXO is present in many coastal, riverine, and estuarine environments throughout the world. Increasingly, people are using these areas for commercial, residential, and recreational purposes. Detecting and characterizing UXO in these underwater environments can be challenging whether they are buried or proud. However, in spite of the recent advances in UXO detection performance, false alarms due to clutter still remain a serious problem. Because the cost of identifying and disposing of UXO in the United States using current technologies is estimated to range up to $500 billion, increases in performance efficiency by reducing false alarm rates can result in substantial cost savings.

This joint research effort between the U.S. Army ERDC and NRL will extend the current art of 2-D sonar classification methods for detection and classification of proud bottom objects to 3-D buried and/or partially buried underwater objects, and ultimately discriminate between buried underwater munitions and buried clutter. The prior art, patented by Gendron, et al. (2), detects mine-like objects in acoustic imagery and classifies them as either mines or clutter based on object dimensions, acoustic shadows, brightness and shape. Classification accuracy for an object is improved, and the probability of false detection is reduced by utilizing different data gathered by the same and/or additional sensors. A spatial search algorithm, based on predicted positional error, helps to ensure that the same object is being considered. A wavelet neural network based feature-matching algorithm is then used to combine the different sensor images and complete the classification (3) Finally, an area-matching algorithm, based on rigid data association methods, aligns adjacent objects to increase mine classification accuracy and reject clutter. This algorithm has been shown to have an of over 90% probability of detection, and low false alarm rate, with sidescan sonar imagery.

Materials and Methods

From the above-mentioned prior art, this project accomplished the following tasks: obtain previously collected sensor data, select a test site, model acoustic / electromagnetic (EM) response of buried munitions, and design the Munitions and Clutter Classifier (MACC). This section describes these accomplishments in more detail.

Obtain previously collected sensor data

Various types of sub-bottom data collected around Duck, NC, were obtained in the first quarter of 2010. Table 1 lists each data type, the instrument used to collect it, along with location, resolution, and age. The table also lists whether the data will be used to select specific test site locations at Duck, or as input data to the MACC for clutter/UXO discrimination. Dr. Jesse McNinch (ERDC MACC P.I.) provided both the SWATHPlus and Edgetech data. Dr. Herb Nelson (SERDP) provided the magnetic data. Data was collected from both the Albermarle Sound and the Atlantic Ocean, off the coast of Duck, NC. Figure 1 shows four Atlantic survey sites: Southern Shores (SS), Kitty Hawk (KH), Sea Ranch (SR), and Nags Head (NH).

Table 1. Data collected to date.

Data type	Instrument	Source	Information	Site Selec-tion	MACC Phase I Input	Location	Resolution	Age
Bathymetry	SEA Ltd. SWATHPlus	McNinch (ERDC)	Bottom Morphology	X		Atlantic Side, Duck, NC	1m - 10m	6-8 yrs
Acoustic Backscatter	SEA Ltd. SWATHPlus	McNinch (ERDC)	Sediment Type	X		Atlantic Side, Duck, NC	1m - 10m	6-8 yrs
Chirp Subbottom Seismic	Edgetech 216i	McNinch (ERDC)	Subbottom	X	X	Atlantic Side, Duck, NC	20 cm (Vertical)	6-8 yrs
Chirp Subbottom Seismic	Edgetech 216i	McNinch (ERDC)	Subbottom		X	Sound Side, Duck, NC	20 cm (Vertical)	< 1 yr
Magnetic Data	Marine-towed Array (MTA)	Nelson (SERDP)	Magnetometer		X	Sound Side, Duck, NC	N/A	5 yrs

Before NRL could begin designing MACC, software routines were required to read the various data types. Dr. Gendron (NRL) wrote the initial algorithms to read and display SWATHPlus backscatter and bathymetry data after consultations with Dr. John Hughes Clarke (University of New Brunswick) and Mr. Bill Danforth (USGS-Woods Hole), both of whom had experience processing these data. Magnetic data collected with the Science Applications International Corporation (SAIC) Marine-towed Array (MTA) at Duck, NC, was obtained from Dr. Herb Nelson (SERDP). Routines were developed to read and convert the data into ARC ESRI shapefiles for display purposes. Magnetic dipoles produced by proud and buried metallic objects can clearly be seen in Figure 2.

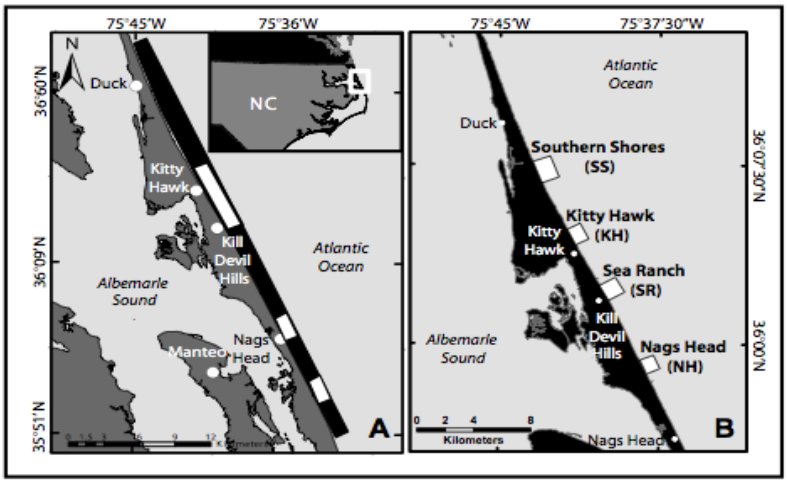

Figure 1 . Maps showing locations of study area and data coverage: A) Bodie Island, NC. Black box indicates extent of data coverage area for 2002 acoustic survey (Interferometric bathymetry & acoustic backscatter and high-resolution CHIRP sub-bottom seismic).). White boxes indicate regions with highly variable surficial and sub-bottom geology. B) Potential focus sites (white boxes) for this study and the location of acoustic time series data from 2002-2004 (4)

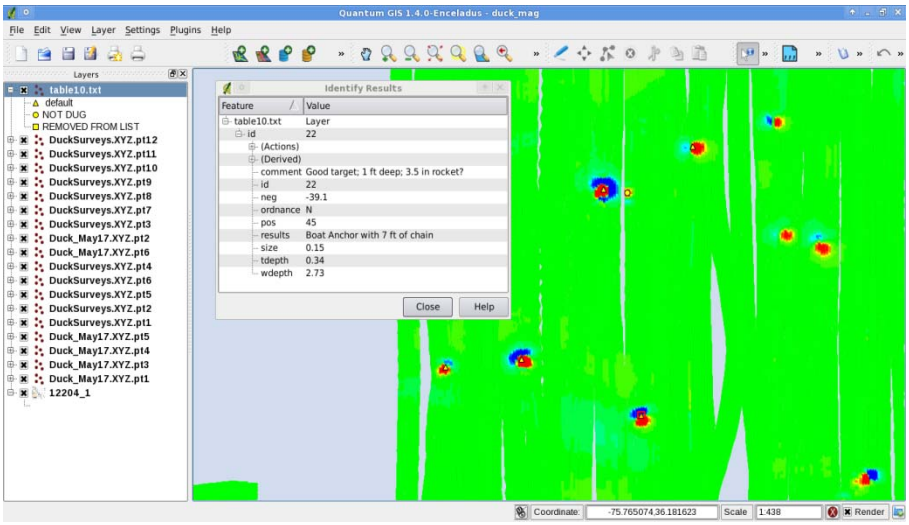

Figure 2 Shapefile of MTA magnetic data clearly shows the magnetic dipoles (red and blue) produced by metallic objects. Data inversion can estimate object depth, orientation, and size.

High-resolution Chirp sub-bottom data was also obtained from ERDC (Figure 3). The greatest variability in the geometry seems to occur in the top two meters of the bottom. This challenging environment is one reason why Duck, NC, was chosen as the test site.

Figure 3 Images of CHIRP high resolution sub-bottom data from Kitty Hawk (A) and Sea Ranch (B). Despite the fact that penetration is on the order of ~5m, significant variability in the geology is found in the upper 2 m of the seafloor *(from Miselis and McNinch, in prep.)*

Test site selection at Duck, NC

Next, Dr. Miselis and Dr. Gendron evaluated the data obtained, including bathymetry, acoustic backscatter, and chirp sub-bottom seismic data, to choose optimal test sites for the MACC. They were interested in regions with diversity in both the data and environments (e.g., sound vs. ocean). The four Atlantic sites represent a variety of nearshore geology and bathymetric variability, as shown in figure 4. The Southern Shores (northern-most) and Nags Head (southern-most) sites drop off steadily from the shore out to sea. In contrast, the Kitty Hawk and Sea Ranch (middle two) sites have highly variable nearshore geology.

The Atlantic sites also have widely varying surficial geology (sediment types), as illustrated in figure 5, from gravel to fine-medium grained sand types ensuring a wide variety of acoustic backscatter strengths. Again, the wide variety of environmental data suggests these will be good test sites for the MACC. As shown in figure 3, the chirp sub-bottom seismic data collected at the Kitty Hawk and Sea Ranch sites reveal significantly variable sub-bottom data (upper 2 m).

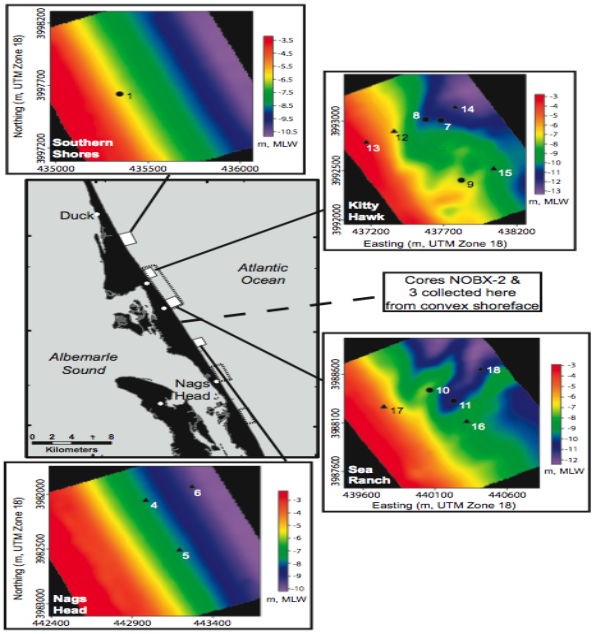

Figure 4 Map of study area and plots of interferometric bathymetry from the regions indicated by the white boxes. Bathymetry is color-coded from warmer colors (shallow areas) to cooler colors (deeper areas). Dashed black lines indicate regions of highly variab variable nearshore geology. Note the Kitty Hawk and Sea Ranch sites are located within one of those regions. Numbers and symbols indicate the locations where vibracores were collected in 2005 *(from Miselis and McNinch, in prep.)*

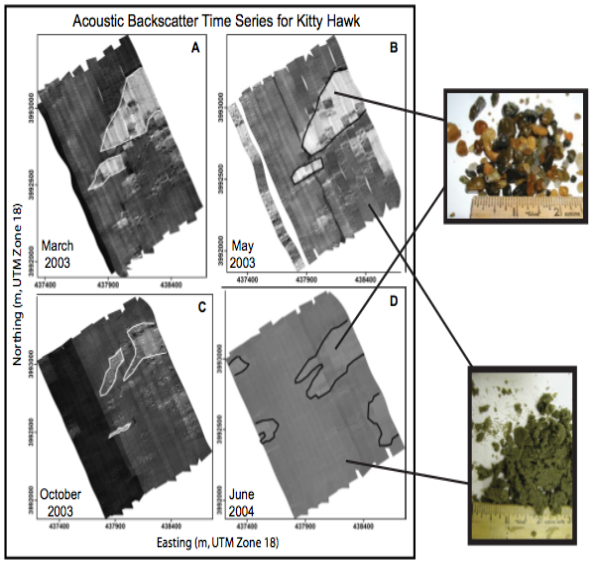

Figure 5 Plots of acoustic backscatter from the Kitty Hawk site from March 2003 (A) through June 2004 (D). Lighter colors indicate higher amplitude returns, and darker colors indicate lower returns. Grab samples taken from the seafloor surface indicate that gravel is present on the shoreface in the lighter regions, while fine-medium grained sand is present in the darker regions (insets). These data demonstrate how variable the surficial geology can be in the study area *(from Miselis and McNinch, in prep.)*

In May 2010, Dr. Gendron, Dr. Miselis, and Ms. Lohrenz (NRL 7441 section head) visited with ERDC investigator Jesse McNinch at the U.S. Army Field Research Facility (USACE-FRF) at Duck, NC. Each agency briefed current work relevant to this project, including automated methods for detection and classification (Dr. Gendron), and a background and current capabilities of the FRF (Dr. McNinch). The investigators conducted a one-day at-sea field test onboard the FRF Light Amphibious Reconnaissance Craft (LARC, figure 1), including a test of the FRF X-Star bottom/sub-bottom profiler in the littoral zone off the FRF site. The team selected several sites in the region, representing a wide variety of nearshore geology, surficial geology (sediment types), sub-bottom types, and bathymetric variability.

Figure 6 Army Field Research Facility (FRF) Light Amphibious Reconnaissance Craft (LARC)

Test site selection was finalized in June 2010. Three MACC test sites were selected to represent the spatial variability in physical and geological characteristics of coastal areas that may be encountered during future UXO remediation. All three sites are in close proximity to the USACE-FRF, which is equipped with unique vessels and field equipment essential for the successful completion of this effort. In addition, several existing datasets have been collected near the facility enabling a thorough understanding of the physical environment before any equipment would be deployed. Finally, the proximity of the FRF to several physically and geologically distinct sites will allow for extensive testing of the classification products, which will ultimately result in more robust classifications for munitions and clutter.

The first site (5) is off the western coast of the island near the FRF in Currituck Sound (Figure 7). That portion of the sound is fetch-limited to the east and west, limiting the growth of waves when the wind comes from those directions. In a recent study in which waves and wave spectra were measured for six months (Oct. 2001-Apr. 2002), wave heights ranged from 0.08-0.59 m (6). Because waves are small, it is expected that temporal changes in seafloor morphology at this site

will be limited. However, there is spatial variability in morphology. Water depths at site 1 range from 1.8-2.4 m, but the presence of shallow shoals (depth ~0.6 m) have been noted. (7) The low energy water conditions and limited bathymetric changes of this site will limit environmental clutter and make this location suitable for initial testing of the MACC.

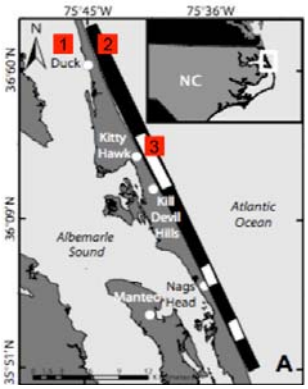

Figure 7 Three sites selected for MACC field tests.

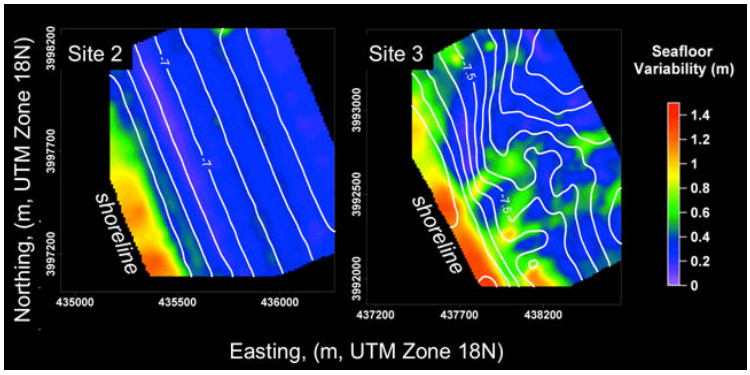

Figure 8 . Bathymetry (contours) and variability (colors) for sites 2 (left) and 3 (right). Adapted from Miselis & McNinch (in prep).

Because of the relatively small distance between the two ocean sites (sites 2 and 3), both experience similar meteorological conditions (Figure 7). The wave and current energy at these sites is higher than at site 1, and therefore, morphologic changes are more dynamic. Tides are semi-diurnal with a mean range of ~1 m (5) and a spring tide range of ~1.2 m (7). The average significant wave height from 1980-1999 is 1.1 ± 0.6 m, as reported on the FRF website (8) (http://www.frf.usace.army.mil/). However, there are significant differences in the morphology and sediment variability between these sites, which will contribute to differences in the degree of environmental clutter. Previously collected interferometric swath bathymetry shows that site 2 has a shore-parallel sand bar, while site 3 has shore-oblique sand bars (Figure 8, contours). This increased variability in the gradient of the seafloor in the alongshore direction at site 3 has the potential to alter the grazing angle of acoustic soundings, which could increase the amount of environmental clutter detected by the MACC. Furthermore, acoustic backscatter and grab samples collected from each site indicate distinct changes in seafloor sediment type over very short distances (< 500 m) at site 3 (Figure 9). The effect of variability in the return intensity of

acoustic seafloor soundings on the successful classification of buried munitions could be tested at this site.

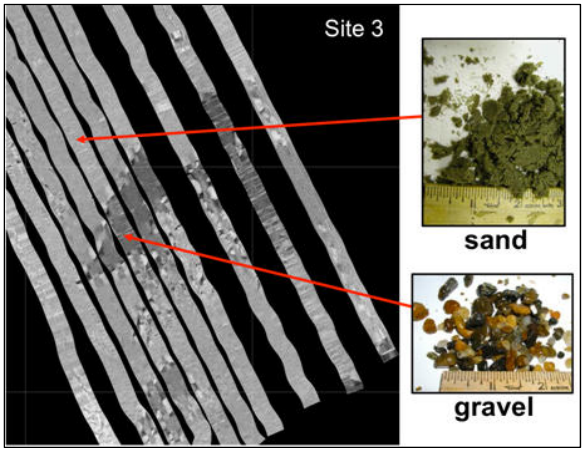

Figure 9 Acoustic backscatter (left) and photos of grab samples (right) for site 3, illustrating the variability in sediment type at the seafloor.

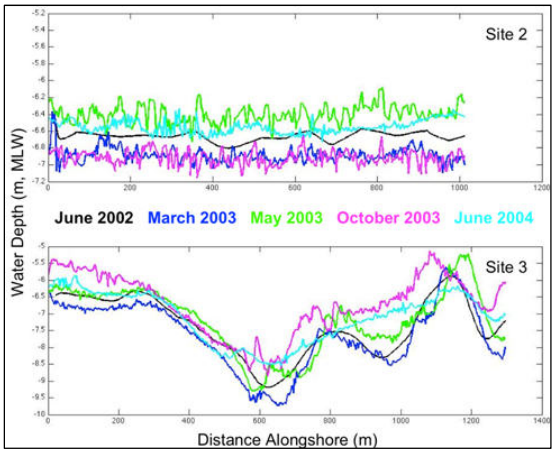

Figure 10 Temporal morphologic changes at sites 2 (top) and 3 (bottom). The scale of the y-axis of the upper panel spans 2m while it spans 5m on the lower panel. Adapted from Miselis & McNinch (in prep).

In addition to having alongshore variations in seafloor gradient and sediment type, site 3 also experiences more dramatic morphological changes than site 2 (Figure 8, colors and Figure 10). The magnitude of bathymetric variability is not only higher at site 3, but it also occurs across the nearshore zone (Figure 4, colors). In contrast, at site 2, the variability is concentrated close to shore. Figure 10 shows the small-scale variability at the two sites. It is important to note that while the bathymetric changes at site 2 are more or less uniform in the alongshore direction (on the order of ~ 0.6 m), the magnitude of changes at site 3 vary from 0.3-2 m over the same period. These findings illustrate the dynamic nature of the nearshore zone and highlight that the thickness and character of the sediment above experimental buried munitions will change

through time. Only through testing MACC in a variety of seafloor sites spanning the range of expected environmental clutter from site to site will the skill of MACC be thoroughly tested.

Model EM response of buried munitions/clutter

In order to optimize the investment of MACC development, we leveraged magnetic data and model results produced in previous SERDP efforts and used these findings to develop plans that would incorporate future EM model products. NRL investigator Will Avera proposed to use EM modeling software, developed at the University of Utah, which uses integral equation formulations for EM solutions. Our efforts have demonstrated the utility of magnetic and EM model products when combined with acoustic products for munitions discrimination, and can be used to establish baselines to build a normalized test bed. Specifically, we can model the EM responses from buried, small, rectangular metallic objects, such as those that could be detected from simple EM metal detector technology. Ferrous magnetic response of similar objects to predict the response of magnetic sensors can also be modeled, such as the magnetic sensor array on the SAIC MTA.Model 3-D acoustics response of buried munitions/clutter

High frequency (20-75kHz) normal incidence sonars have in recent years increased their capability to the point they may detect and characterize buried objects of various scales and depths. However, as detection capabilities advance, the problems associated with differentiating objects of interest from naturally occurring scatterers become greater. Hence, classification of targets based on the scattering from buried objects becomes a major component of the solution.

Options for characterizing the returns from acoustic scatterers can roughly be separated into spectral or imaging methods. If the wavelength of the acoustic signal is small compared to the size of the target, the object may be imaged to such a fine resolution that its shape or structure may be revealed. This is often accomplished using a wide bandwidth (high temporal resolution) signal. Otherwise, if the wavelength of the acoustic signal is large compared to the target size, spectral methods are often employed. These utilize relatively narrowband methods (with good spectral resolution) designed to identify characteristic resonances or nulls in spectra.

However, practical factors place bottom penetrating sonar systems squarely in the middle of these two domains. Hence, time-frequency analysis becomes a viable option for characterization of scattering from buried objects. Time-frequency analysis in the form of Wigner-Ville and Choi-Williams distributions were investigated characterizing the acoustic scattering from buried objects. Comparison of modeled and tank-collected data demonstrated the utility of time-frequency analysis in characterizing specific acoustic interactions. Salient features of scattering were revealed in the time-frequency distributions that were not easily identifiable in either time domain or frequency domain only analysis.

Time-frequency analysis techniques, in conjunction with time domain or frequency domain techniques, were applied to interpretation and characterization of scattering from free-field and buried solid cylinders. This was applied to a particular case where practical constraints common to bottom penetrating systems (limited bandwidth, temporal separation from surface returns, low signal-to-noise ratio) result in a severely limited amount of information to analyze. Without the

constraints of dealing with buried objects, much more detailed information (more spectral resonances and nulls, or more distinct echoes) would be available, making characterization of the object relatively more robust. However, for buried targets, one must deal with a paucity of information. Some of the constraints in dealing with buried objects may be ameliorated (such as reducing system noise), but some (such as the bandwidth) are definite limits to the amount of information available. It may be possible to increase the useable bandwidth over the 1 octave used in this analysis, but with increasing attenuation with frequency, one expects diminishing improvements with such an increase.

In this study, cylinders of two sizes were analyzed with an acoustic model and tank measurements. Only the larger cylinders exhibited elastic interactions. The system noise (transients from amplifier turn-on and turn-off) somewhat corrupted the signals, particularly for the buried cylinders, but differences between the two objects were still discernable. Reduction or elimination of this source of noise (which has been achieved since original preparation of the manuscript) would certainly enhance the process of identifying specific acoustic interactions in addition to those shown in this analysis. Higher order modes, which show up after the main pulse echo, would be more evident in a less noisy signal. But they are also generally weaker. Surface borne modes (Lamb waves), which would be helpful in characterizing an object, are also likely to be easily obscured by volume reverberation. Further refinement of technology is required to reveal the extent to which acoustic interactions in buried objects can be characterized.

Modeling was also used to show that time-frequency analysis produces a descriptive picture of targets, which can be the basis for classification of objects. Principal component analysis (PCA) was applied to the time-frequency distributions in order to discern the most pronounced distinguishing features. Even when the object was modeled as a rigid scatterer, PCA revealed discernable differences between the two objects. Moreover, PCA retained information concerning elastic interactions in the model of the larger cylinder. PCA was not presented for the observed data, due to corruption from transients.

Model and data comparisons were generally consistent. Some unexpected differences were observed, most notably, in the apparent slope of the specular reflection in the time-frequency distributions. Whether this is misrepresentation of a physical phenomenon by the model or a clue to a system problem is key to the concept that a buried object can be characterized solely by the specular reflection.

Modeling Component -- Scattering From Finite Cylinders

One of the topics of this limited scope project was to model the acoustic response of simulated munitions and compare that to measured responses. It was determined that finite metal cylinders would make an acceptable inert object to test against given the similarity in size and shape between some munitions and finite cylinders. The important information question to answer was, are there sufficient features measureable in the acoustic response of these objects to aid in classification of the objects?

Phenomenological Description

Scattering of plane waves by elastic cylinders in the free-field (in an unbounded fluid medium) is a well understood problem with exact numerical solutions (9) . However, a phenomenological description must resort to either a ray based description or a wave based one. In either case, the most significant interaction is the specular, or mirror-like, reflection off the front of the cylinder. Once energy penetrates the cylinder, two modes of propagation (faster compressional and slower shear waves) are generated. Waves of either type bounce around within the cylinder, reradiating sound as they impinge back on the surfaces of the cylinder, resulting in multiple weaker echoes successively delayed with respect to the specular reflection. Surface waves are also generated. These are relatively weak and slow moving waves that travel around the surface of the cylinder (10).

Scattering by buried elastic cylinders is complicated due to two factors: the water-sediment boundary (thus, for shallowly buried objects, multiple scattering between this boundary and the object may be significant), and the surrounding elastic medium. When embedded in an elastic medium, the cylinder is being radiated by compressional and shear waves (not necessarily plane waves, even if they could have been considered so in the water column). Moreover, a surrounding elastic medium causes more complicated surface born waves around the cylinder than in the case of one surrounded by a fluid (11). See (12) (13) for a more complete treatment of scattering from buried objects.

Description of numerical model

Scattering from cylinders has received much attention for many years within the acoustic literature. Due to the symmetry of the problem, modal solutions in the far field are exact for plane wave incidence and have been verified with experimental measurements for various materials (9). Limiting cases of these theories yielded several approximate solutions (14). The analysis presented in this paper uses Stanton's model (15) with some modifications appropriate for the observing system in question. Because it treats the ensonifying energy as a plane compressional wave, it neglects shear waves within the sediment. In addition, interactions between the water-sediment interface and the cylinder are ignored.

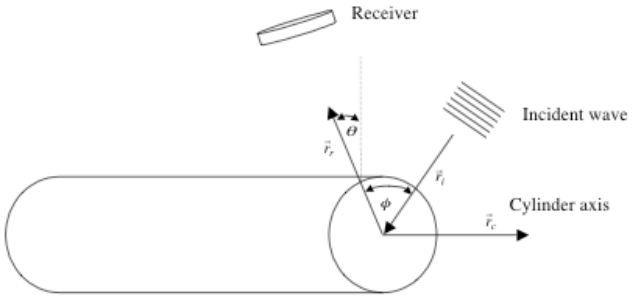

Figure 11 Geometry for scattering model

Following Stanton's treatment, this analysis begins by examining the pressure due to a small segment of an infinitely long line of point sources (in that energy is reradiated by the cylinder) of

narrow band (with acoustic wavenumber *k*) energy. This is integrated to determine the scattered field for a cylinder of finite length *L* and radius *a*. Here two assumptions are worth noting. First, scattering from the ends of the cylinder is ignored. Within this analysis, the ensonifying beam is treated as Gaussian, so this assumption is valid if the cylinder is longer than the footprint of the ensonifying beam. Secondly, for the cylinder to appear acoustically to be of finite length, the receiver-target separation r must be great enough for the cylinder to be within the first Fresnel zone. For the frequencies treated here (20-75 kHz) and the separation assumed (at least 5 m), this assumption is valid. Stanton (Eq. (6) in (14)) shows that the differential pressure uniformly integrated over an interval –*L*/2 to *L*/2 yields

$$P_{scat}(k) = -P_0 \frac{L\, e^{ikr}}{\pi\, r} \frac{\sin(\Delta)}{\Delta} \sum_{m=0}^{\infty} \varepsilon_m \sin(\eta_m) e^{-i\eta_m} \cos(m\phi) \qquad (1)$$

Here P_0 is the amplitude of the incident plane wave, *r* is the source-target separation, Δ is $\frac{1}{2} kL(\vec{r}_i - \vec{r}_r) \bullet \vec{r}_c$, $\vec{r}_i$ is the unit normal in direction of plane wave, $\vec{r}_r$ is the unit normal in the direction of receiver, $\vec{r}_c$ is the unit vector pointing along the axis of the cylinder. This geometry is illustrated in Fig. 11. ε_m is Neumann's number (ε_0=2, ε_m=1 for *m*>0), and ϕ is the azimuthal angle. η_m is a scattering phase angle. See (14) following Eq. (1) for detailed formulation of η_m in terms of the elastic properties of the cylinder, wavenumber, and geometry. For a rigid cylinder η_m simplifies to

$$\tan(\eta_m) = -\frac{J'_m(ka)}{N'_m(ka)}. \qquad (2)$$

J'_m and N'_m are derivatives with respect to the argument of Bessel functions of the first and second kind, respectively, for order *m*.

However, for the system treated here, the length parameter *L* and the *k* space amplitude beam pattern, $\sin(\Delta)/\Delta$, is replaced by the equivalent for ensonification by a Gaussian beam. At a distance *s* from the maximum response on the bottom, the beam pattern along the length of the cylinder is

$$v(s) = e^{-s^2/2\sigma^2}. \qquad (3)$$

Here σ is a length parameter derived from the half-power beam-width. The amplitude-weighted effective length ensonified by a Gaussian beam is

$$\hat{L} = \sqrt{2\pi}\,\sigma e^{-s_0^2/2\sigma^2}. \qquad (4)$$

Here s_0 is the distance from the maximum response on the bottom to the closest point of approach of the cylinder. The *k* space amplitude beam pattern, $\sin(\Delta)/\Delta$, in Stanton's treatment is obtained from the Fourier transform of the beam pattern $v(s) = \sin\theta$ between –*L*/2 and *L*/2, zero

otherwise). However, the beam pattern here is Gaussian. In wavenumber space, it is conveniently also Gaussian.

$$V(k) = \frac{1}{\sqrt{2\pi}\sigma} \int_{-\infty}^{\infty} e^{-2\pi i k s} e^{-s^2/2\sigma^2} ds = e^{-k^2/2\Sigma^2} \tag{5}$$

Here $\Sigma = 1/2\pi\sigma \sin\theta$.

Hence the scattered pressure using a Gaussian beam is

$$P_{scat}(k) = -P_0 \frac{e^{ikr}}{r} \frac{\hat{L}}{\pi} e^{-k^2/2\Sigma^2} \sum_{m=0}^{\infty} \varepsilon_m \sin(\eta_m) e^{-i\eta_m} \cos(m\phi) \tag{6}$$

.

This expression requires a few simple modifications to be useful here. First, the amplitude of the incident plane wave P_0 should be replaced by $P_1 r_0/r$, where P_1 is the magnitude of the transmitted signal, r_0 is a reference range, and spherical spreading to the bottom is assumed (where it is also assumed the bottom is flat enough for the plane wave approximation to be valid). Secondly, bottom effects need to be included. Assuming a flat bottom comprising a homogeneous lossy half-space with sound speed c_s and density ρ_s (sound speed c_w and density ρ_w in the water), the pressure is reduced by the factor $T_{ws} T_{sw} e^{-2\alpha_s z_s}$. Here $T_{ws} = 2\rho_s c_s / (\rho_w c_w + \rho_s c_s)$ is the normal incidence plane wave transmission coefficient from the water to the sediment, $T_{sw} = 2\rho_w c_w / (\rho_w c_w + \rho_s c_s)$ is the same back into the water, α_s is the attenuation coefficient, and z_s is the depth of the cylinder below the surface. The phase in the factor e^{ikr} must also be altered to account for transmission through the bottom, where wavenumbers in the water, k_w, now become $k_s(1+\delta_s)$ in the sediment. The path lengths r_w and r_s correspond to those in the water and in the sediment, respectively, and the factor δ_s is the ratio of the imaginary component of the wavenumber to the real ($\delta_s = \alpha_s / k_s$).

Hence

$$P_{scat}(k) = -P_1 T_{ws} T_{sw} e^{2i(k_w r_w + k_s r_s (1+i\delta_s))} \frac{\hat{L} r_0}{\pi (r_w + r_s)^2} e^{-k^2/2\Sigma^2} \sum_{m=0}^{\infty} \varepsilon_m \sin(\eta_m) e^{-i\eta_m} \cos(m\phi) \tag{7}$$

Neglecting refraction in the bottom in the above treatment introduces minimal error for angles near vertical.

Lastly, it should be noted that this solution is for a continuous wave signal of infinite duration. For a band-limited, finite duration pulse, a time series can be created from Fourier synthesis of solutions over a discrete range of wavenumbers k_n, $n = n_{min}, \ldots n_{max}$.

$$p_{scat}(t_j) = \frac{1}{N} \sum_{n=n_{\min}}^{n_{\max}} S(k_n) P_{scat}(k_n) e^{2\pi i (j-1)(n-1)} \qquad (8)$$

Here $S(k_n)$ are the Fourier coefficients of the chirped pulse $s(t_j)$:

$$S(k_n) = \sum_{j=1}^{N} s(t_j) e^{-2\pi i (j-1)(n-1)} \quad , \qquad (9)$$

where

$$\begin{aligned} s(t_j) &= \exp(2\pi i f_j t_j) \quad t_j < T_p \\ s(t_j) &= 0 \qquad\qquad\qquad \text{otherwise} \end{aligned} \qquad (10)$$

and

$$f_j = f_{\min} + (f_{\max} - f_{\min}) t_j / T_p \; . \qquad (11)$$

In the above, f_j is the instantaneous frequency swept from a low of f_{min} to a high of f_{max} over a time interval T_p, $\Delta k = 2\pi f_s / N c_s$ is the resolution of the wavenumber in the inverse Fourier transform, and n_{min} and n_{max} are determined from the lower and upper frequency bounds. Alternatively, the impulse response is

$$h_{scat}(t_j) = \frac{1}{N} \sum_{n=n_{\min}}^{n_{\max}} P_{scat}(k_n) e^{2\pi i (j-1)(n-1)} \; . \qquad (12)$$

Time-frequency analysis

The standard tool of spectral analysis, the Fourier transform, decomposes a signal into its individual component frequencies. It reveals the intensity of each component, but does not indicate when that component began or ended. The spectrogram was devised to observe the Fourier components over short windowed intervals of time. However, this is only useful if the signal is stationary over the span of the window. Moreover, this diminishes frequency resolution. Time-frequency analysis was developed out of the need to characterize events with concurrent local components in both domains. For an excellent review of the topic, the reader is referred to (16).

The historical roots of time-frequency analysis are from quantum physics. It was a useful tool in bridging the gap between descriptions of particle and wave mechanics. Likewise, in this physical application, it is useful in bridging the gap between interpreting ray and wave descriptions of acoustical interactions. While understanding the roots of these methods, it should be noted that the terminology involving “distribution” does not properly apply in signal analysis, as it did in quantum physics, yet has endured. Herein, objects labeled as distributions should not be interpreted as being probability distributions, but as distributions of energy in the time-frequency domain.

The Wigner-Ville distribution (WVD), describing the intensity of a signal $u(t)$ at time t and frequency ω, is defined as (16)

$$W(t,\omega) = \frac{1}{2\pi}\int u^*\left(t-\tfrac{\tau}{2}\right)e^{-i\tau\omega}u\left(t+\tfrac{\tau}{2}\right)d\tau \quad . \qquad (13)$$

A general method of obtaining this is to utilize the relationship between the power spectrum and the autocorrelation function. By generalizing the definition to that of a time dependent or local autocorrelation function,

$$R(t,\tau) = u^*\left(t-\tfrac{\tau}{2}\right)u\left(t+\tfrac{\tau}{2}\right), \qquad (14)$$

the WVD can be rewritten as

$$W(t,\omega) = \frac{1}{2\pi}\int R(t,\tau)e^{-i\tau\omega}d\tau \quad . \qquad (15)$$

Hence, the WVD can be computed by first generating the two-dimensional local autocorrelation matrix $R(t,\tau)$, and then taking the Fourier transform of each column (across τ). In the following results, where the WVD is shown for modeled signal, the scattered pressure $p_{scat}(t)$ from Eq. (8) is used for the signal $u(t)$ in Eqs. (13) and (14). For the observed data, the received signal is used.

As noted later in presentation of the results, the WVD involves a second order product, resulting in cross-products, which may be misinterpreted as distribution of energy in the time-frequency domain. Techniques, such as using a smoothing function, as with the Choi-Williams distribution, have been developed for minimizing these cross-products, but at the cost of reduced temporal and spectral resolution.

Choi and Williams (17) defined a generalized time-dependent autocorrelation function as

$$R_t(\tau) = \frac{1}{2\pi}\iint w(\xi,\tau)u^*\left(\varphi-\tfrac{\tau}{2}\right)\cdot u\left(\varphi+\tfrac{\tau}{2}\right)\exp\left(i\xi\left(\varphi-t\right)\right)d\varphi d\xi, \qquad (16)$$

where $w(\xi,\tau)$ is a windowing function. Their choice for the smoothing function $w_{CW}(\xi,\tau)$ was

$$w_{CW}(\xi,\tau) = \exp\left(-\left(\xi\tau/\gamma\right)^2\right), \qquad (17)$$

where γ is a parameter controlling the amount of cross-term suppression. The two-dimensional inverse Fourier transform of the generalized time-dependent autocorrelation function yields the Choi-Williams distribution (CWD).

Experimental Exercise

Test Tank

Acoustic scattering data were collected at the National Marine Fisheries fresh-water tank at the Southeast Fisheries Center at Stennis Space Center, Mississippi. This facility is a 1.4 million liter, 11 m deep fresh-water tank. At the bottom was placed a pool containing uniform grain size (8 micrometer) sand 1.4 m deep. A rail system was constructed and placed at the top of the tank to mount a transducer that could be moved perpendicular to the orientation of the targets. This transducer was mounted on a gimbal, which could be mechanically steered along the length of the targets (perpendicular to the rail). A two-axis inclinometer was used to measure the orientation of the transducer. This configuration is illustrated in Fig. 12

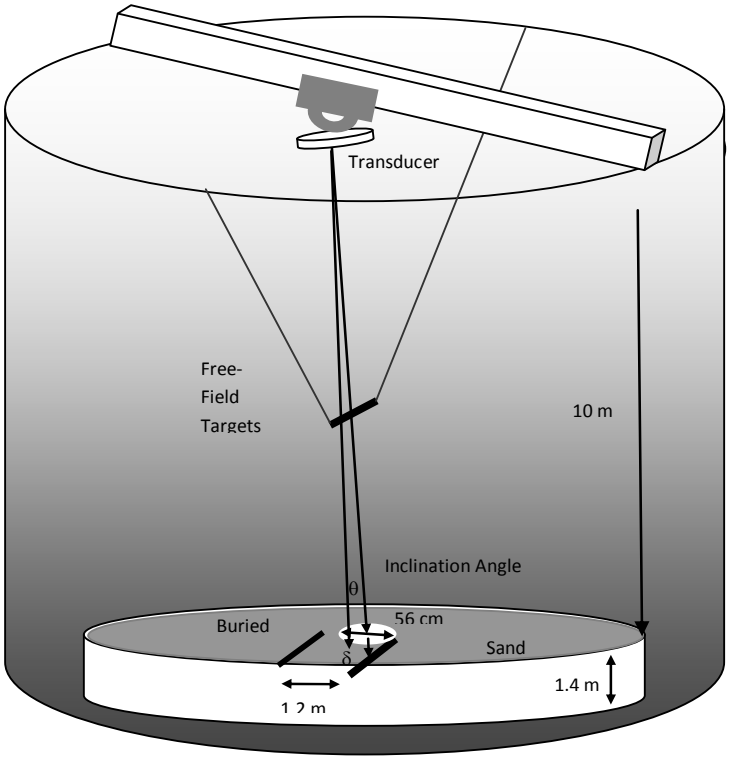

Figure 12 Test set-up at NMFS tank

The 1.3 m long rods were buried in the sand at the bottom of the pool by divers. To do this, the sand had to be liquefied beneath the rods along their entire length. A frame was constructed that allowed water to be pumped around the rods while being forced into the sand. At the desired depth, the frame, unconnected to the targets, was removed from the sand, leaving the target behind. This required about a 20 l/s pump. There was concern that this process might introduce air bubbles into the sand, but no evidence of this effect was noticed in the data collected.

Cores from the sand were taken before and after burial. There was no change in the measured characteristics after burial. The compressional wave sound speed was observed to be 1725 m/s and the density was 2 g/cm^3. Attenuation was measured to be 13.4 dB/m at 400 kHz. This value was consistent with the reverberation observed with the 30 to 60 kHz chirped signal. Measurement techniques are described in (18).

Transducer

The transducer used to acquire the data has been designed and fabricated by Naval Undersea Warfare Center for a narrow beam subbottom profiler system under development at NRL. It is a hybrid design with both a receiver element and transmit element enclosed in the same housing to allow monostatic operation. The receive element is located behind the thin transmit element which is acoustically transparent at the receive frequency. Each element is constructed on 1-3 composite and is roughly square (38 cm on a side). The transmit layer, which is tuned to frequencies near 200 kHz, is plated with 30 linear electrodes that can be individually driven. When phased appropriately, the resultant beam can be steered on one axis. Because of the large aperture and high transmit frequency, a very narrow beam (< 2 degrees) is generated. Each transmit element is driven at a high level (~230 dB re 1 μPa at 1 m) using a signal that consists of the sum of two gated sine waves. Due to non-linear interaction in the water column, a parametric signal is generated at a frequency equal to the difference of the frequencies of the two sine waves. This parametric beam is very narrow (< 2 degrees) and has virtually no sidelobes (< 40 dB). Furthermore, since relatively small changes in the transmit frequency can generate large variations in parametric difference frequency, the parametric signal can be swept across large frequency ranges without moving far from transmitter resonance.

The receive element is thicker and therefore receives in a linear mode with a resonance near 45 kHz. The signal from the receive element is amplified and recorded with a 24 bit A/D converter at a sampling rate of 200 kHz. It is transmitted to the recording and display system via gigabit Ethernet.

Targets

Two targets were used in this experiment, both of which were aluminum rods 1.3 m long. The thinner rod was 2.86 cm in diameter and the thicker 5.08 cm. Travel times for compressional waves propagating through 10 cm samples from each rod were measured using a Panametrics V101 0.5 Mhz 1.0" Videoscan transducer. Travel times for shear waves were measured using a Panametrics V151 0.5 Mhz 1.0" Videoscan transducer. These samples were weighed in order to compute density. Properties for these samples are summarized in Table 2.

Table 2 – Physical properties of aluminum cylinder targets

Property	Thin Rod	Thick Rod
Diameter (cm)	2.86	5.08
Length (m)	1.3	1.3
Compressional Speed (m/s)	6179	6234
Shear Speed (m/s)	3089	3062
Density (g/cm^3)	2.73	2.73
Burial Depth (cm)	37	55

Processing

The targets were ensonified by the parametric sonar with a 30 to 60 kHz linear frequency modulated signal with 0.25 ms duration. The primary frequencies of the parametric sonar were swept symmetrically about a center frequency near 200 kHz to generate the chirped difference frequency. There was a 10 μs ramp up and ramp down at the beginning and end of the signal, resulting in a small loss of bandwidth. The impulse response is obtained by deconvolving the received signal with a source wavelet. The source wavelet was obtained by placing the source transducer on the bottom of the test tank and pointing at the surface. The surface reflected signal was observed, and used to compute a zero-gain inverse filter for deconvolution, which is carried out in the frequency domain. The Fourier transform of the signal is multiplied by a window function to reduce sidelobes, then divided by the inverse filter. The inverse Fourier transform results in the impulse response. In the case of an infinite bandwidth, this process would ideally result in an infinitesimally short impulse. However, given imperfect observation of the source wavelet, and a limited bandwidth, the best achievable impulse response is one of finite duration having significant side-lobes.

For each data set, the source was placed over the target and the amplitude of the received signal was maximized by successively steering the beam across the target (over inclination angle θ), and translating the transducer along the rail system. The position at which the amplitude was maximized was taken as normal incidence. At this position, multiple (~1000) pulses were averaged in order to get a single time series. The averaged time series were deconvolved in order to produce an impulse response. But the averaged time series (prior to deconvolution) were used for time-frequency analysis.

Results

In each of Figs. 13-17, 20-23, three plots are shown. In each, a time-frequency distribution (either Wigner-Ville or Choi-Williams) is shown in the upper right corner with frequency as the horizontal axis and time as the vertical. Below that is a power spectrum along the same frequency domain. To the left is an impulse response along the same time domain. In the case of modeled data, the spectrum is given (except for a scaling factor) by Eq. (7). Also shown for comparison (dashed line) is the approximate target strength (TS) for a finite length rigid cylinder at broadside incidence (14), computed using

$$\mathrm{TS}(k) = 10\log_{10}\left(\hat{L}^2 ka / 4\pi\right) \qquad (16)$$

The impulse response, computed from a limited range of wavenumbers, is acausal. It should be noted that the same dynamic range (20 dB) is used on all plots.

Also shown in each of the following displays is the impulse response, given by Eq. (12), for the model results and by the inverse-filter method described in section IV.D, for the observed data. The magnitude is displayed as sound pressure level (SPL) relative to 1 μPa. To compute this, the source level is assumed to be 191 dB re 1 μPa at 1 m uniformly across the frequency range 30 to 60 kHz. The time-frequency distribution reveals how, both temporally and spectrally, the chirped signal is reflected by the target.

Model results for the smaller 2.86 cm diameter free-field rod are shown in Figs. 13 and 14. First, the elastic model is used (Fig. 13). Then, for comparison, the rigid model is shown (Fig. 14). Also shown for comparison in Fig. 15 is the echo off a point scatterer. These plots indicate that, for the signal used here, this target can be treated as a rigid material. That the WVD comprises only a single linear distribution of energy means that little acoustic interaction other than specular reflection occurs. The impulse response shown in Fig, 13A indicates a temporally local event. The side-lobes are artifacts of Fourier synthesis of a band-limited signal, not necessarily indications of discrete acoustic events, such as distinct echoes, as one might expect for larger cylinders. The power spectra (Fig. 14C) also show few features other than a slight dip in power in the middle of the band. In sum, there is no visible indication of any elastic behavior in this smaller target.

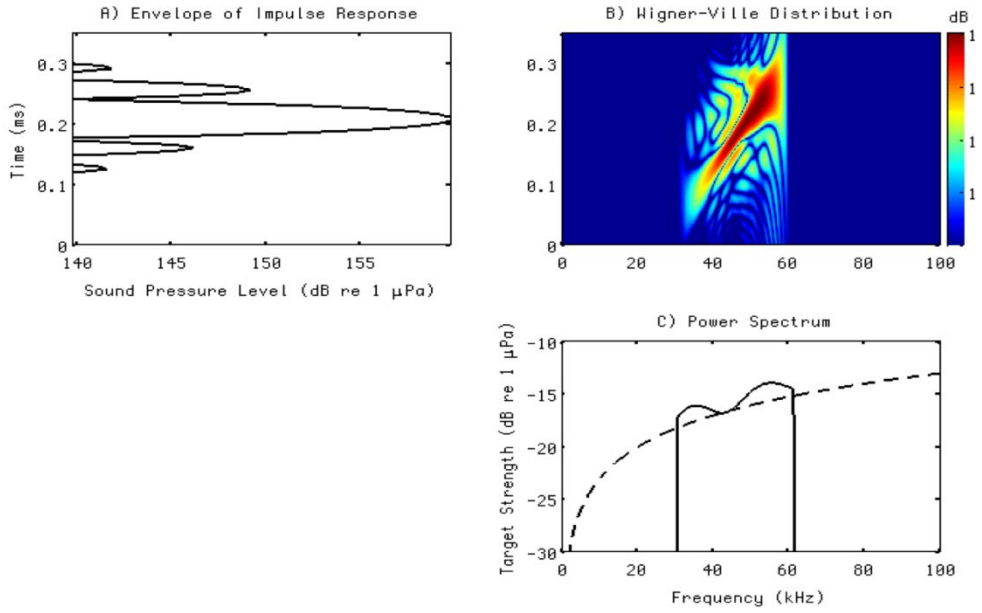

Figure 12 Elastic model of scattering from small cylinder in free-field

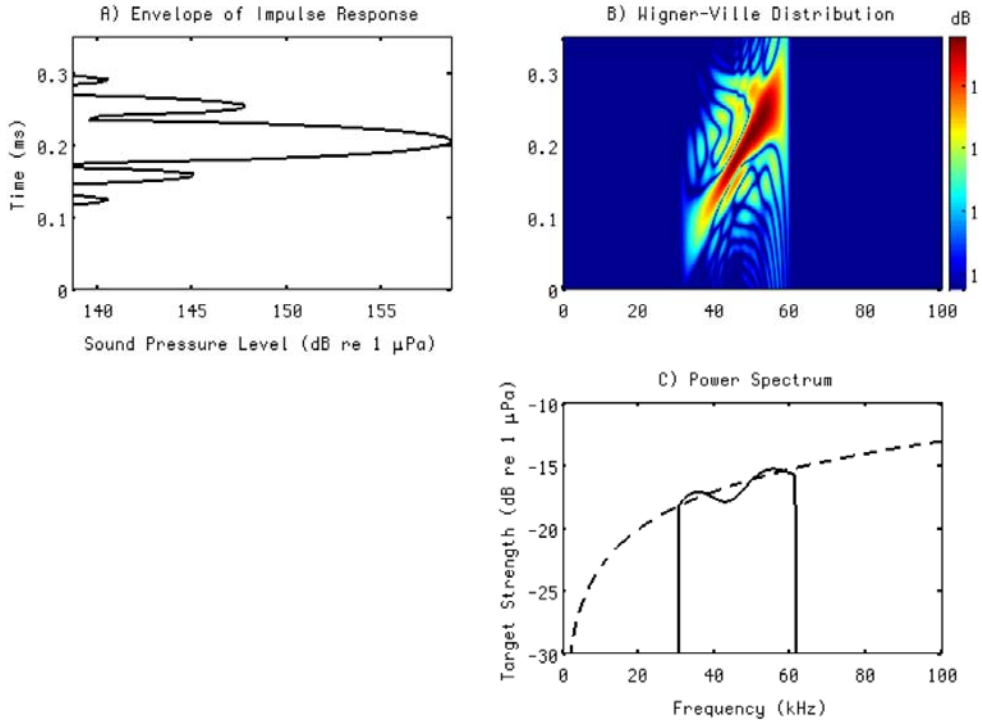

Figure 13 Rigid model of scattering from small cylinder in free-field

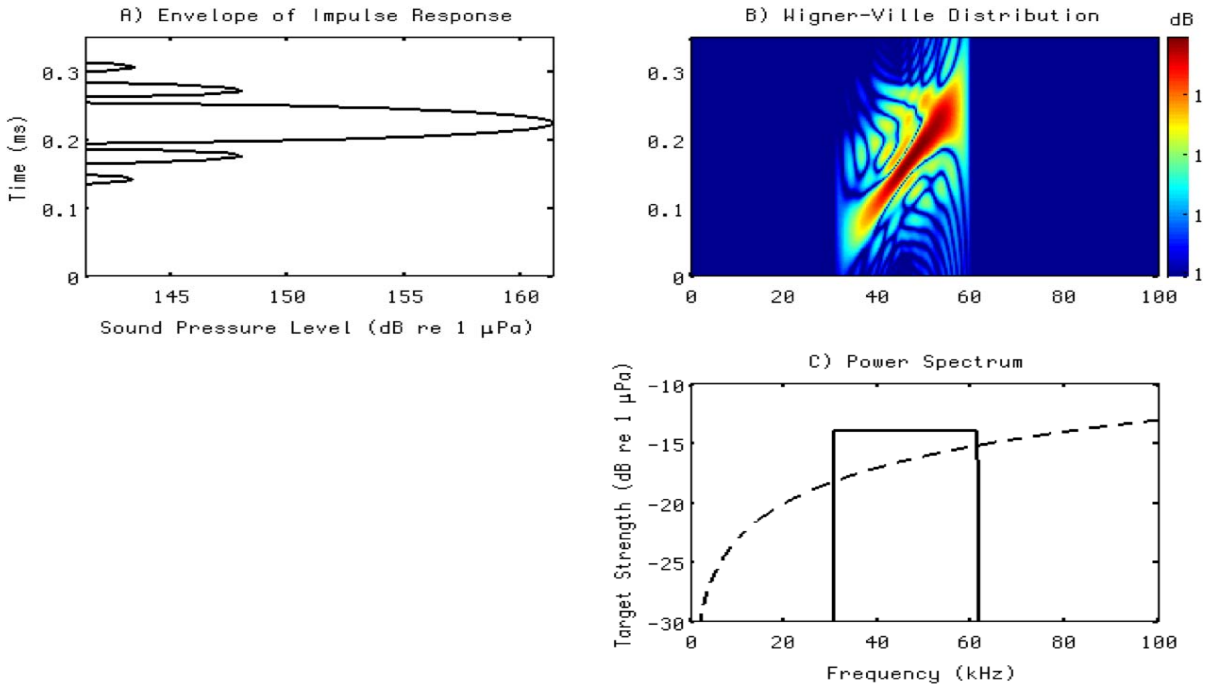

Figure 14 Model of scattering from point target in free-field

In contrast, model results for the 5.08 cm diameter free-field rod are shown in Figs. 16 and 17, for the elastic and rigid models, respectively. These reveal a more complex situation than the previous example. Most notably, the power spectrum for the elastic case (Fig. 16C) shows deep nulls at 46 and 56 kHz. These are due to destructive interference between compressional and shear waves within the cylinder. The impulse response (Fig. 16A) likewise reveals a second discrete event occurring 50 µs after the specular arrival. These features are revealed in the WVD (Fig. 16B) as groups of energy off the main diagonal distribution of energy, and as gaps in energy along this line. As mentioned in section III, each distinct group of energy appearing in a WVD does not necessarily correspond to a separate identifiable acoustic interaction. To suppress the effect of cross-products within the distribution, Choi Williams smoothing was applied. The effect of smoothing is shown in Fig. 18, in which a CWD is computed with $\gamma^2 = 0.1$.

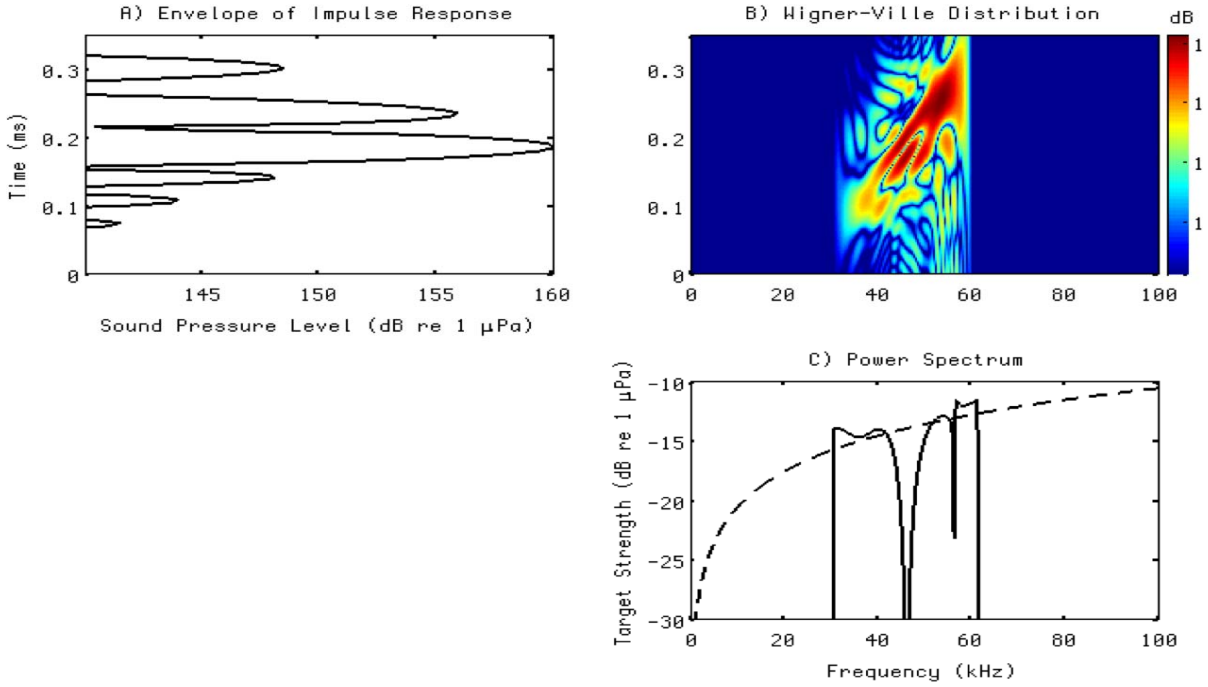

Figure 15 Elastic model of scattering from large cylinder in free-field

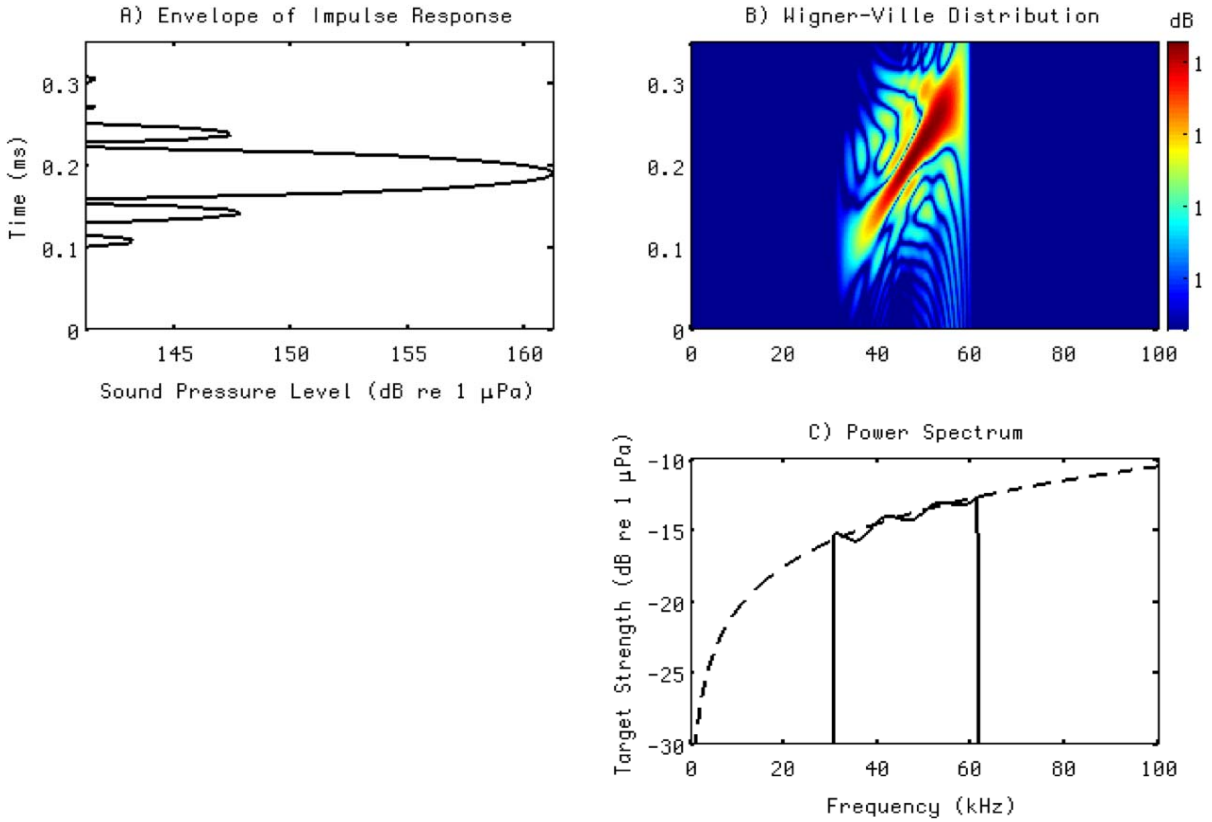

Figure 16 Rigid model of scattering from large cylinder in free-field

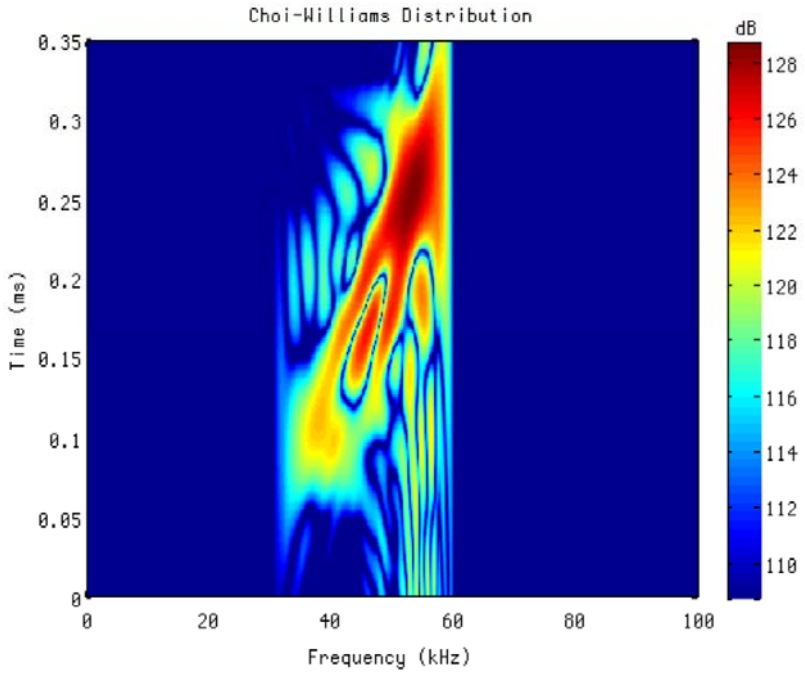

Figure 17 Choi-Williams distribution for elastic model of large cylinder in free-field

Principal component analysis (PCA) was used on the time-frequency distributions in order to further interpret the differences in acoustic interactions between the two targets, and also to investigate the effect of smoothing. PCA is a technique used to reduce a problem of large dimensionality to a lower dimension problem amenable to easier interpretation (19). In this case, it is hypothesized that a small number of principal components can be extracted that account for the specular reflection and the small number (if any) of elastic effects.

The first 10 principal components (PCs) of the time-frequency distributions are shown in Fig. 19. Prior to PCA, each distribution was normalized by its maximum. Those for the elastic model are plotted with a '+', for the rigid model, an 'o', and the one for the CWD of the elastic model, an 'x'. In all cases, at least 99% of the variance is accounted for using the first 6 PCs. By removing the first few PCs, it was confirmed that these do indeed account for the specular component. By comparing the rigid (blue 'o') and elastic (blue '+') model PCs for the smaller rod, no significant differences are noticeable. However, for the larger cylinder, the second through fifth PCs are noticeably different for the elastic model (red '+') than the rigid model (red 'o'). Thus the principal component analysis is successful in depicting elastic effects, when present. Moreover, comparing the second through fourth PCs of the rigid models for the two different size rods (blue 'o' vs. red 'o'), some differences are noticeable. Hence, even a difference in the specular reflection can differentiate the two.

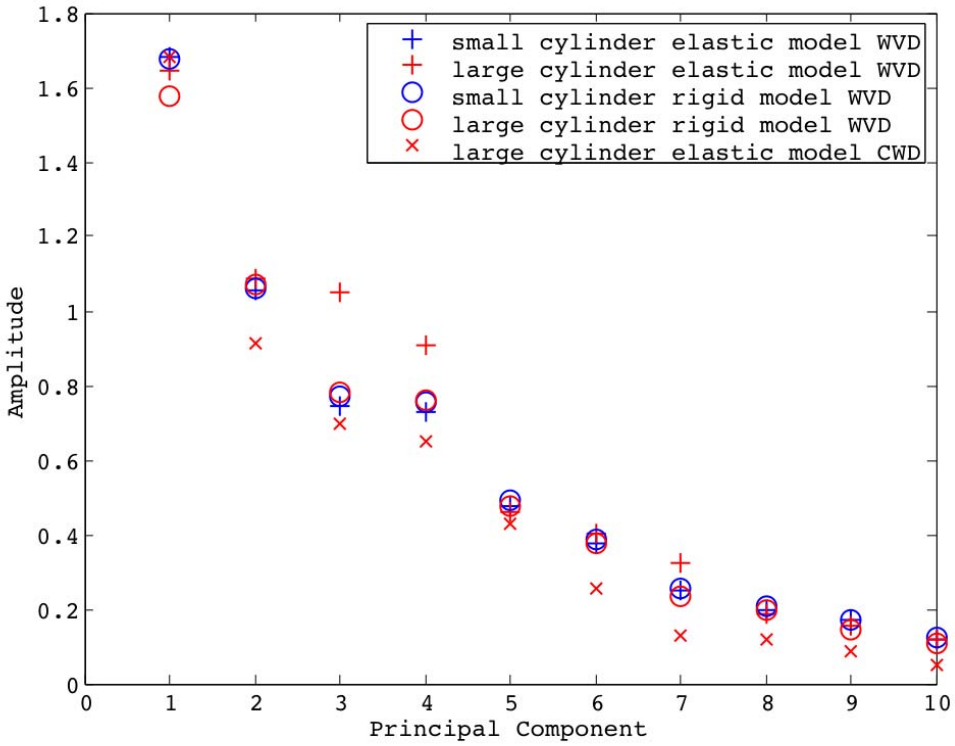

Figure 18 PCA of T-F distributions for modeled signals

The PCs of the CWD for the elastic model of the larger cylinder are shown (red 'x') in Fig. 19. Elastic effects are more evident in this larger cylinder, as seen in the WVD of Fig. 16, are retained in the CWD of Fig. 18, and are also preserved in the PCA. In the second through fourth PCs, where elastic effects are evident, Choi-Williams smoothing has no effect on the second (as compared to the WVD - red '+'), but reduces the level of the third and fourth. This indicates that these components in the WVD are indicative of cross-terms, rather than physical acoustic interactions.

Observed data for the 2.86 cm diameter free-field rod are shown in Fig. 20. The actual echo here is of longer duration than the modeled signal. It had been noticed that the amplifiers, which are gated-on just prior to pulse generation, and off afterwards, were generating transients seen spectrally as wide band noise. The turn-off transient shows up at the end of the pulse in Fig. 20, but does not overlap it. The linear sweep pulse is the portion of the signal from .08 to .23 ms in Fig. 20B. Being incoherent with the chirped pulse, it does not appear well in the deconvolved impulse response (Fig. 20A).

As with the model predictions, no elastic interaction is visible. The power spectrum (Fig. 20C) reveals few distinguishing features, as does the impulse response (Fig. 20A). The latter is broader than that predicted, by a factor of two. This is due to the windowing used in

deconvolution. A similar window was not used in the model in a desire to predict the best possible temporal resolution. The CWD (Fig. 20B) is similar to the modeled distribution (Fig. 13B), in that it is dominated by the specular reflection. However, in the CWD of the observed data, the slope of the chirped signal is slightly greater than that modeled (note the .5 ms extent of time scale for the observed data is longer than the .35 ms duration used for the modeled data, due to the interference from the transients). That the slope is distinctly different than that expected from the model reveals a fundamental deficiency of the model.

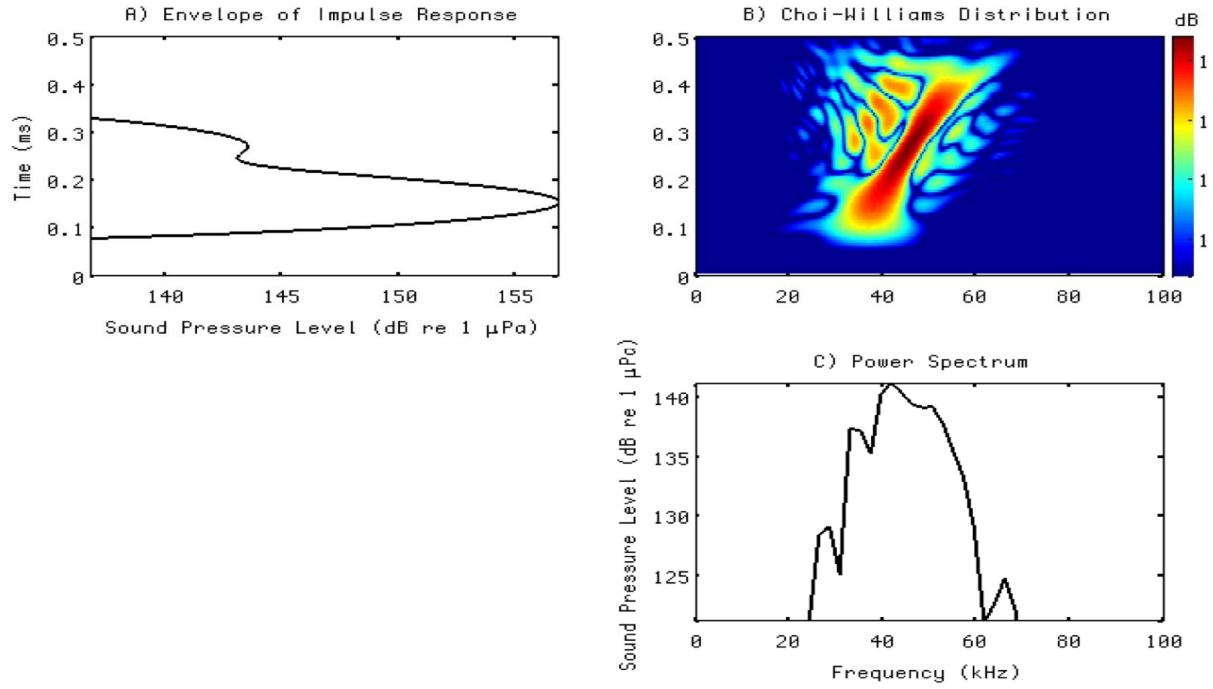

Figure 19 PCA of T-F distributions for modeled signals

Likewise, some of the features seen in the observed data for the 5.08 cm diameter free-field rod shown in Fig. 21 are similar to model predictions. The power spectrum (Fig. 21C) does indeed reveal a deep null. The impulse response (Fig. 21A) also reveals features indicating multiple interactions, but these are harder to distinguish than in the ideal case (compare to Fig. 16A). In the CWD of the actual data (Fig. 21B), the turn-off transient again follows the end of the chirped pulse (from .1 to .35 ms). The interference effect seen as a null at 46 kHz in the spectrum shows up as an off-diagonal features in the CWD. It should be noted also that the SPL (and correspondingly, the target strength) for this case is lower that for the 2.86 cm diameter rod. It is also lower than that predicted by the model.

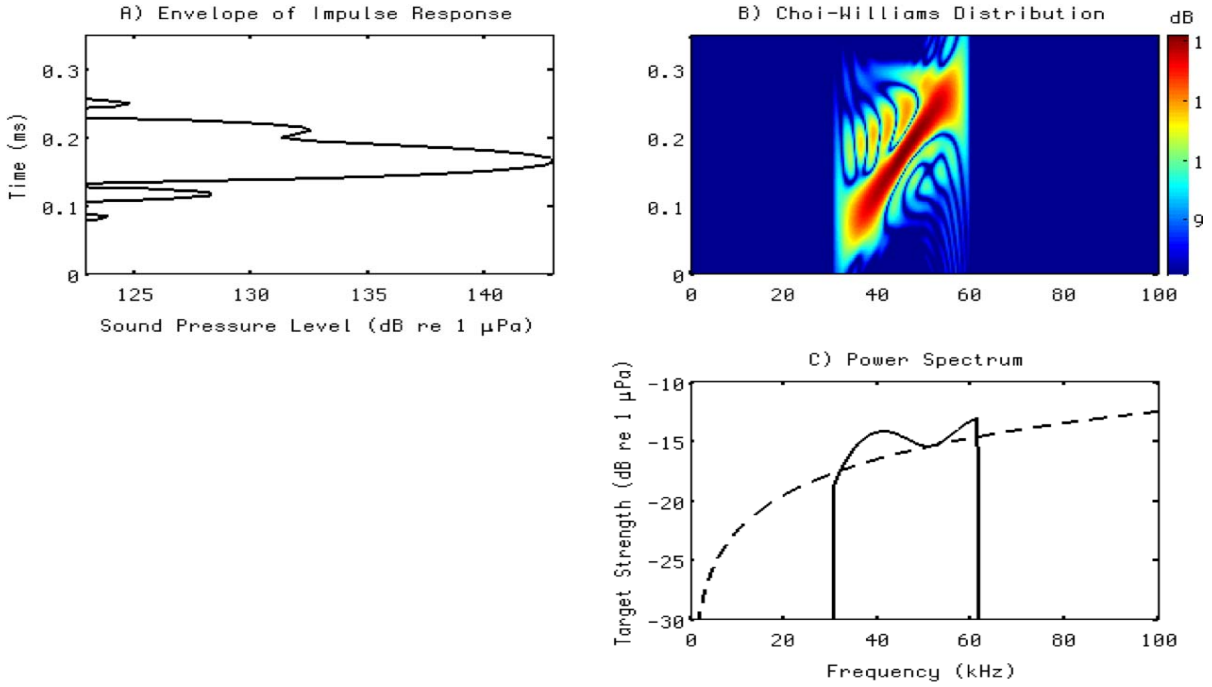

Figure 20 Observed scattering from large cylinder in free-field

The model for the 2.86 cm diameter rod buried to .37 m depth (to top of rod), shown in Fig. 12, indicates that this target still acts mostly as a rigid object. The main effect of burial is to shift the slight null in the spectrum upwards.

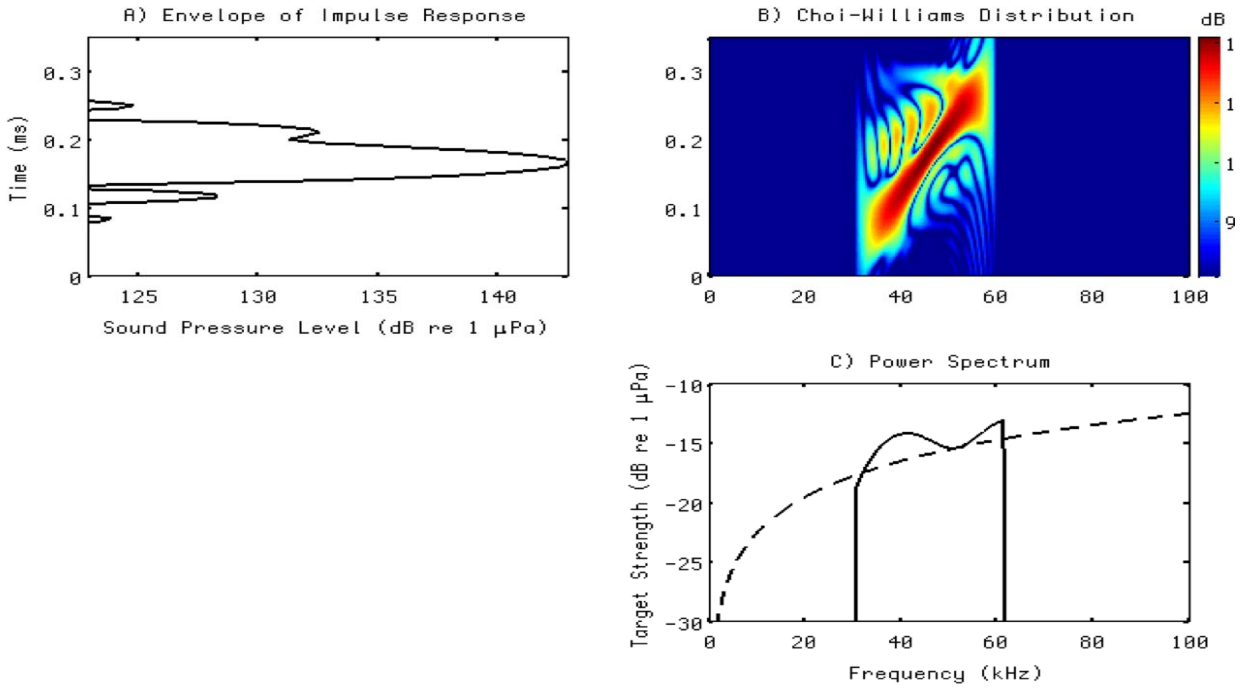

Figure 21 Elastic model of scattering from small buried cylinder

In contrast, model results for the 5.08 cm diameter rod buried to .55 m depth, shown in Fig. 23, indicate more pronounced effects of burial. The power spectrum (Fig. 23C) shows the nulls at the same frequencies as in the free-field case (Fig. 16C), but here the energy in between is suppressed. This yields a weaker TS (and received SPL) than with the thinner rod. The CWD (Fig. 23B) is also distinctively different than in the free-field case (Fig. 16B). As opposed to the free-field case, where most of the energy is concentrated in the later, high-frequency part of the sweep, in the buried case, it occurs in the early, low frequency part. In the middle region, the interference feature resulting from elastic interactions is still pronounced.

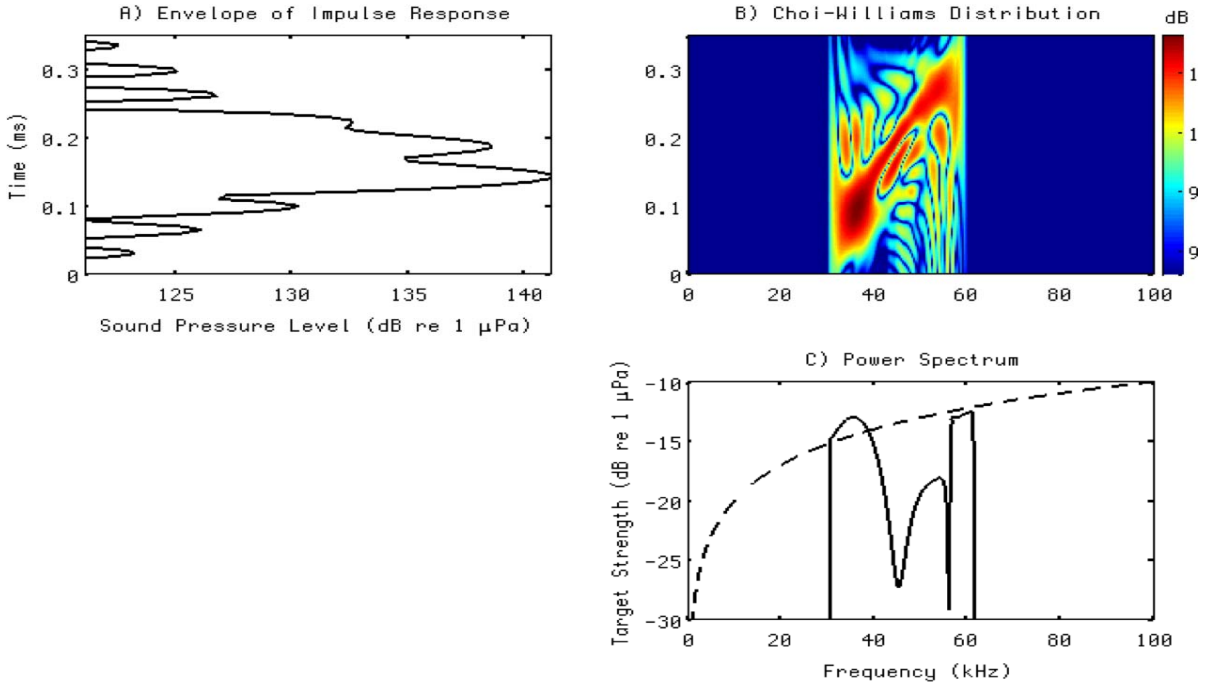

Figure 22 Elastic model of scattering from large buried cylinder

Observed data for the buried targets expose more difficulties in dealing with time domain data. The observed data for the 2.86 cm diameter rod buried to .37 m depth (to top of rod), shown in Fig. 24, is further contaminated by remnants of the return from the water-sediment interface. This is visible in the impulse response (Fig. 24A) and the CWD (Fig. 24B). The specular return is easily distinguishable in the impulse response, but little else can be inferred from this time-domain data. The SPL is 5 dB less than predicted by the model (Fig. 22A), which may be attributed to poor penetration into the sediment due to surface roughness. Although divers attempted to smooth out the sand after burial of the rods, significant surface deformations were visible. This resulted in variations in the intensity of the surface returns of 6 to 12 dB within a span of only a few meters distance. Hence it is not expected that the levels observed for buried cylinders will be close to those modeled. It is notable that there is significant energy below 30 kHz for the buried target. This is noise from the amplifier transients and shows up more prominently for the buried targets than for the free-field targets.

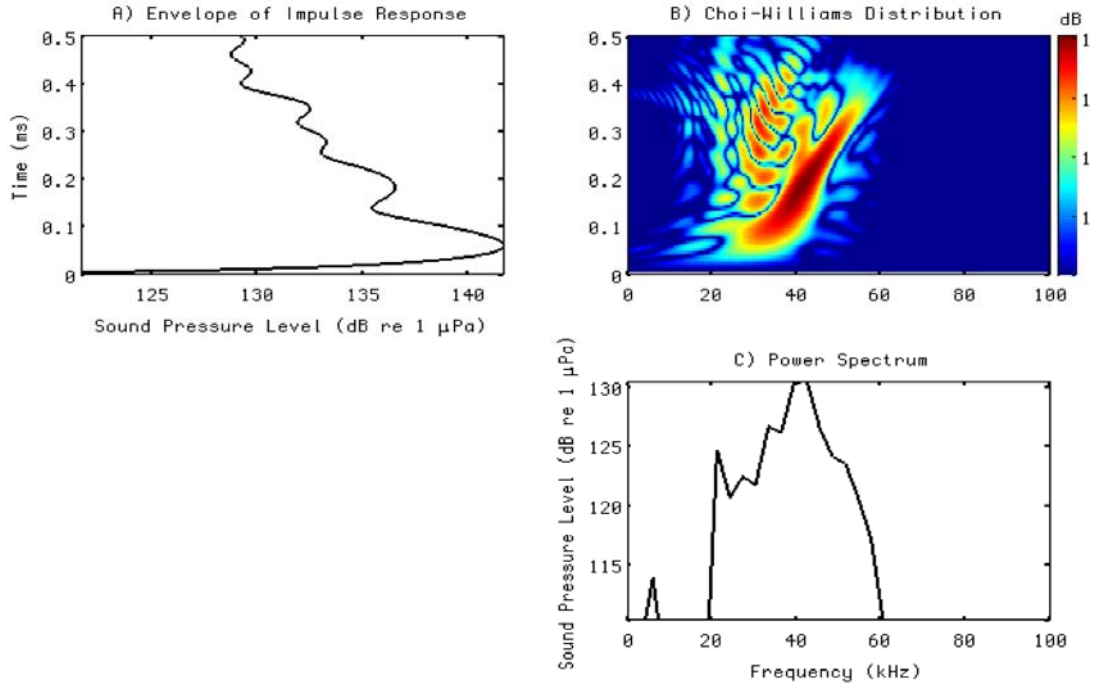

Figure 23 Observed scattering from small buried cylinder

Observations of the 5.08 cm diameter rod buried to a depth of .55 m, shown in Fig. 25, continue to reveal complex interactions. However, this return is very weak. Even though the model predicts noticeable elastic interactions, the same interactions result in a lower target strength. As with the thinner rod, the impulse response (Fig. 25A), being somewhat obscured by the surface return, reveals little information. The SPL is close (142 dB at its maximum) to that predicted (141 dB, see Fig. 23A). The CWD for the buried 5.08 cm diameter rod (Fig. 25B) reveals some of the off-diagonal interference effects as that predicted (Fig. 23B). Again, there is significant energy below 30 kHz resulting from system noise.

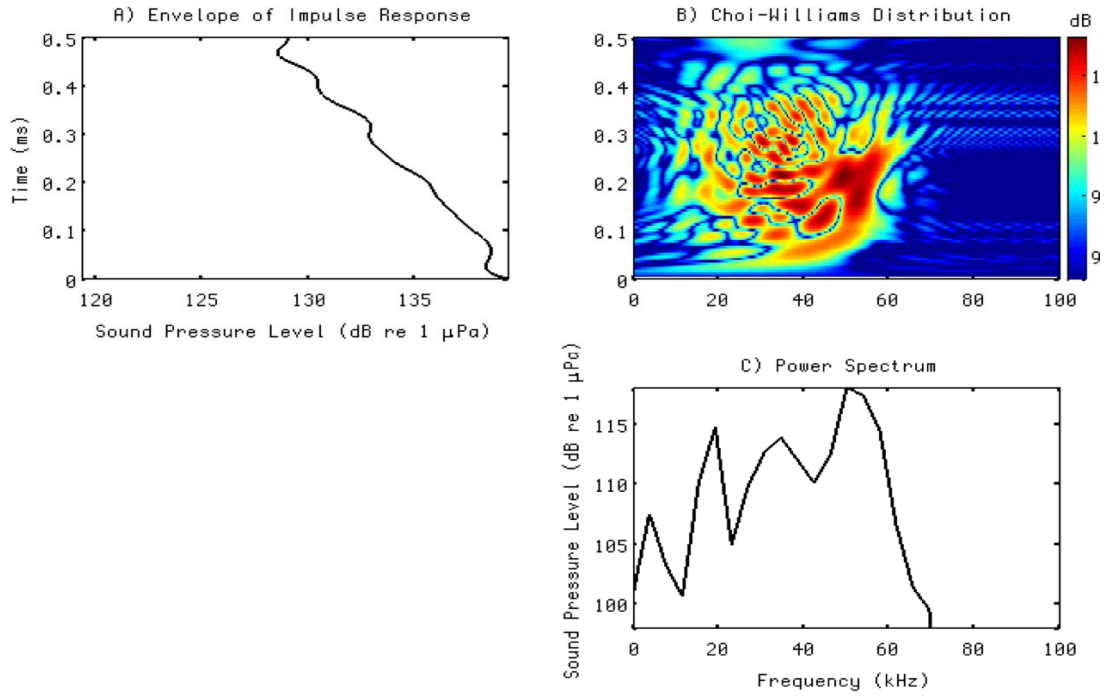

Figure 24 Observed scattering from large buried cylinder

Field Results

The downward looking parametric transducer and receiver described above was used in a field test in the Gulf of Mexico. One example of an automatic detection of buried objects from this system is shown in figure 26. In this example, two different oil and gas pipelines buried several meters deep were detected. The bottom was mostly mud. Some layering is evident, likely sand deposited in storm events. The surface echo in figure 26 extends for several milliseconds, making detection of objects in the first few centimeters difficult. However, after the surface echo subsides, buried targets return a strong enough echo to be discriminated from the background volume reverberation. In this example, the surface above the buried object appears flat and relatively undisturbed. However, other detections (not shown) from this trial revealed surface expressions, either burial troughs or sudden changes in the reflectance of the surface return.

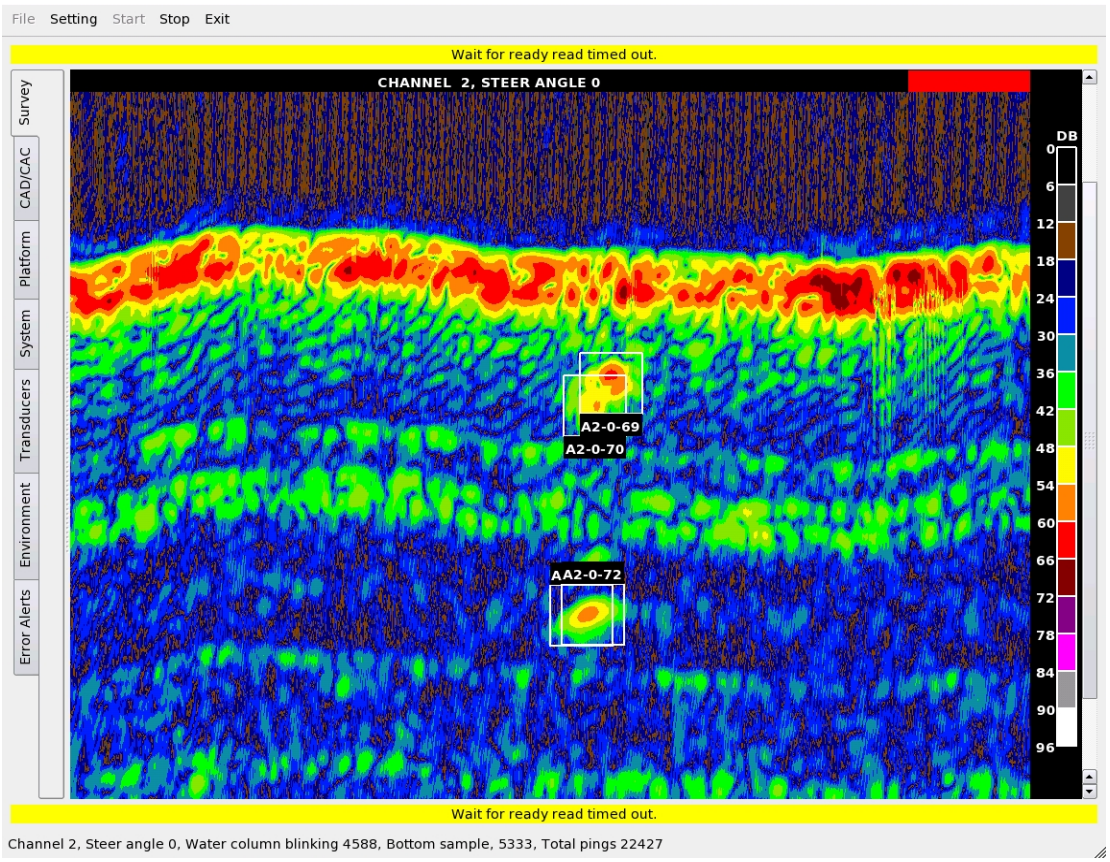

Figure 25 Cylindrical objects found in sediment.

Develop Munitions And Clutter Classifier (MACC) Phase I

MACC, when completed, will be a set of automated algorithms capable of discriminating UXOs from clutter buried below the seafloor. Before discrimination can occur, MACC needs an Automated Target Recognition (ATR) algorithm. For a previous project, Dr. Gendron (NRL MACC P.I.) developed an ATR for the Naval Oceanographic Office (NAVOCEANO) that works with sidescan imagery stored in a specific data format (the NAVOCEANO UNISIPS format). For SERDP this quarter, NRL modified Gendron's ATR to be more generic by removing all dependences on UNISIPS. The ATR now accepts data in a common format and allows easy input of sensor-specific metadata. Finally, a plug-in for the NRL/NAVOCEANO Environmental Post-Mission Analysis (EPMA) system was also designed and implemented for the ATR, such that testing and modification of the ATR with sub-bottom data (Table 1) could begin.

During a naval exercise in June, 2010, Dr. Gendron tested and validated the ATR algorithms (as EPMA plug-ins) that will be adapted for the MACC. As part of the ATR validation process, the team developed an Acceptance Test Procedure, which was successfully completed by naval

personnel during the exercise. According to the Commander, Naval Meteorology and Oceanography Command (CNMOC), "… the data fusion and analysis required less time than the data collection. In the past, analysis required on average, four times as long as data collection… with the new system, the [data fusion and analysis] time required is 0.7 as much."

In October of 2010 an analysis of results from the naval exercise was completed. Specifically, it was determined that the Automated Change Detection and Classification – Real-Time (ACDC-RT) system, and its associated ATR algorithms, performed very well with REMUS sidescan sonar data provided for the exercise. Requiring little to no operator input during a search, ACDC scanned the baseline data for contacts, compared all new contacts to the baseline database, and determined which contacts were historical and which were new. ACDC-RT detected approximately 75% of contacts that had been manually detected by the Naval Oceanography Mine Warfare Center (NOMWC) team. Figure 27 shows the ACDC GUI, complete with four detections that were compared to the aforementioned baseline database.

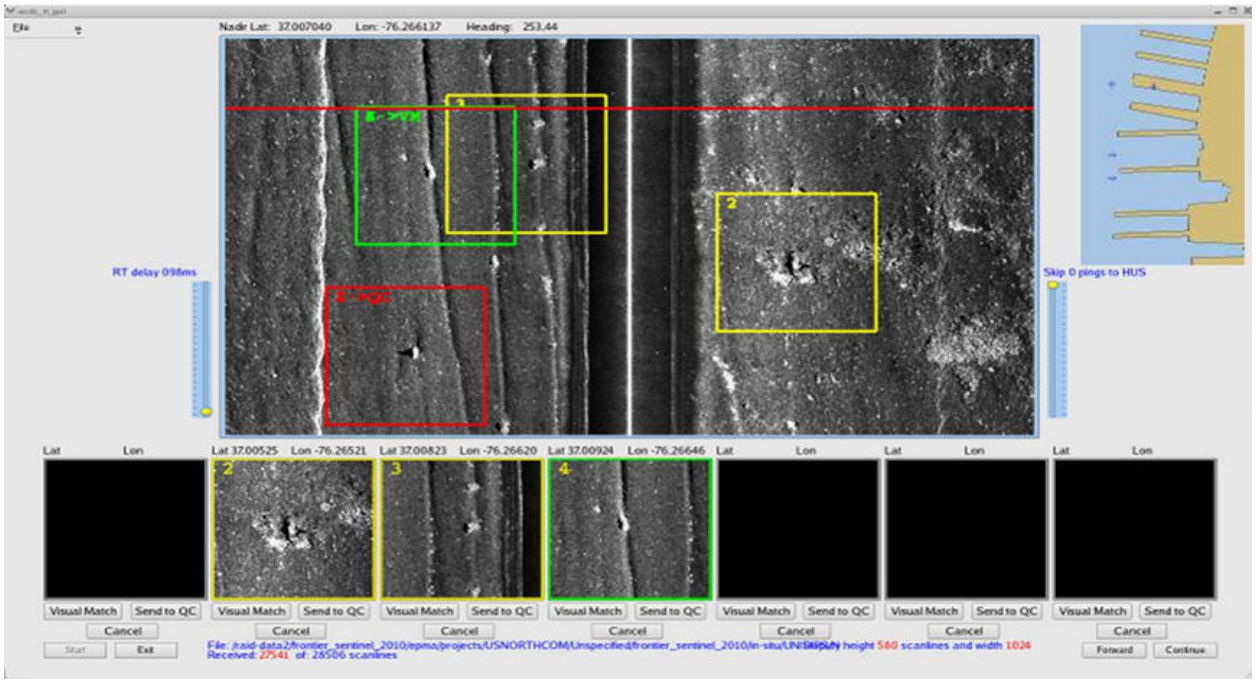

Figure 26 The four boxes indicate detections to be compared, the map in the upper right shows new contacts that can be passed along to MEDAL or a GIS such as HarborSuite, and the red line indicates the line at which the algorithms are being run.

Next, the ATR algorithms developed for ACDC-RT were evaluated for their usefulness with other data types and systems, which could be used in a follow-on SERDP effort. In particular, these algorithms were incorporated into the Target and Change Detection (TCD) Center, developed by the Naval Surface Weapons Center-Panama City Detachment (NSWC-PCD), along with other tools including:

1) The Common Operator Interface for the Navy (COIN), developed by SeeByte to aid operators performing change detection;

2) HarborSuite, developed by Triton Imaging Inc., which specializes in fast access and organization of large volumes of seabed images for continual monitoring of port environments;

3) The ATR Testbed developed by NSWC-PCD, which consists of a package of algorithms that scans sonar images for all possible features of interest;

4) Coherent Change Detection algorithms being developed by NSWC-PCD, which apply radar-based inter-scene coherence between multi-temporal images to reliably detect the appearance of small man-made objects in SAS imagery; and

5) SureTrak, developed by Naval Air Systems Command (NAVAIR), along with the Automated Warning and Response Engine (AWARE), which combine to form an Integrated Battlespace Visualization and Decision Support Tool.

Following the unexpected death of Dr. Gendron, the next steps toward developing the MACC were reevaluated. Dr. William Sanders and Mr. John Dubberley (both of NRL) consulted and produced a preliminary design for a clutter classifier using Bayesian inference to determine how to properly combine the various detection sensors to maximize the likelihood and accuracy of detection. Since the detector would still be tuned to avoid missing munitions detections, there would still be a large number of false targets to prosecute. Support Vector Machine classifiers would then be used to classify the targets as munitions. The high level design is illustrated in figure 27.

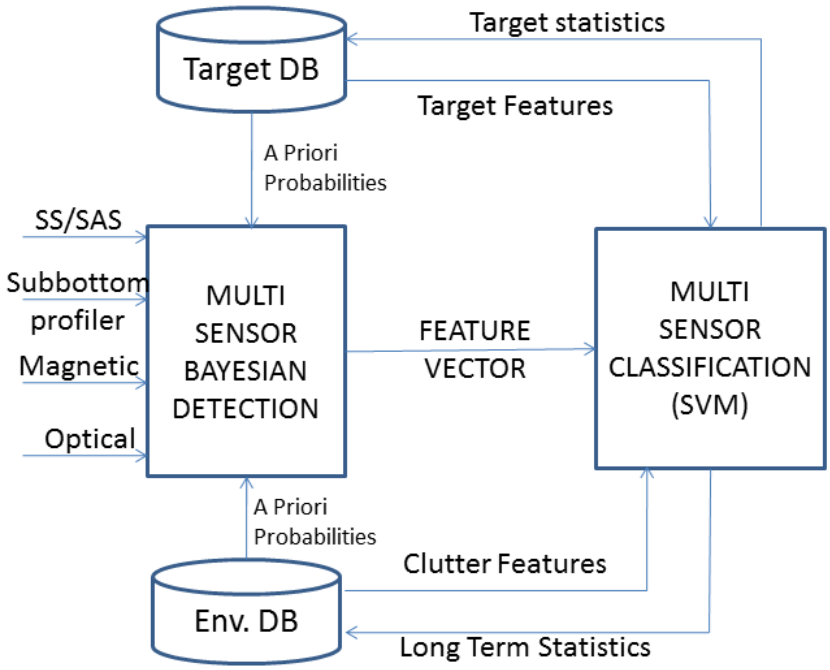

Figure 27 Munitions and Clutter Classifier Schematic

Bayesian inference is a method of combining inputs from different sources to choose the most likely of a set of two (or more) hypothetical options. It is an optimal weighting of the inputs that minimizes the risk of making a wrong decision, based on a prior assessment of probabilities of the separate hypotheses and the relative importance of the various outcomes. The Bayesian framework can be applied to the detection and classification problem separately, or as a single inference problem. The result of a Bayesian inference solution is not just the choice of the most likely hypothesis, but an assessment of the probability of each possible outcome. Hence, treatment of uncertainty is a natural element of Bayesian inference.

Future work will develop a test-bed that uses Bayesian inference to separately treat the detection, localization and classification capabilities within a reconfigurable multi-sensor network of sensors. For any configuration, the goal will be to 1) construct a maximum likelihood detector, 2) minimize localization estimation errors, and 3) minimize errors in feature vector estimates.

We anticipate applying new classification algorithms, based on Support Vector Machines (SVM), that take advantage of the feature vectors calculated by the detection sensors. Feature vectors may include magnetic properties, surface expressions detected in sidescan imagery or sea floor characteristics derived from the side scan imagery , and optical imagery when available. Using a known training set developed in the test field, the object characteristics will be clustered into UXO categories (e.g. 105mm shell) and non-UXO bottom object (e.g. anchors, oil drums, or pipes) categories in a randomly chosen 90% of the available data. The classifiers' performance on the remaining 10% of the data will be used as a metric scoring the skill of the classifier. New detected objects are classified by their closeness of fit to each grouping. Grouping centroids can be adjusted dynamically as new data is entered.

We expect that the findings of the test-bed will support the design of a classification framework for underwater features of interest based on the following principles. As in medical image analysis, statistical classifiers will be used to determine maximum separation classes in a feature space formulation of a feature-based dataset composed of the labeled detections from test detections at Duck. Common machine learning classifiers to be investigated include back-propagation neural networks (BPNN) and SVM.

Performance of a classifier can be improved by aggregating modalities and designing an optimal feature space to describe individual features, in this case, underwater objects of interest. This classification framework will combine the downward-looking sonar imagery with extrapolated morphology and with other available imagery as a feature space. This feature space would improve the classifier's ability to discriminate among morphology classes, such as man-made objects and natural formations. The NRL investigators will design and implement this classification framework, optimize the classification feature space, and collect metrics on classification performance.

Results

The team was able to obtain sufficient previously collected sensor data for the purposes of this limited scope project. After completing the site survey, two test sites were selected which met the test range criteria. A method of obtaining EM response of buried munitions was found.

Extensive modeling of the 3-D acoustic response of buried objects was done. Most importantly a preliminary design of the Munitions and Clutter Classifier (MACC) was accomplished.

It was found that practical constraints common to bottom penetrating acoustic systems (limited bandwidth, temporal separation from surface returns, low signal-to-noise ratio) result in a severely limited amount of information to analyze. For buried targets, one must deal with a paucity of information. For the smallest objects, there was little evidence that there were elastic interactions at all, making discrimination from naturally occurring point scatters (clutter) virtually impossible, given the bandwidth and power constraints for that sonar. Even for larger targets, where elastic interactions were evident, there were still a limited number of features available for classification. These features coupled with magnetic responses should be sufficient for classification of larger munitions.

In addition, several publications linked with this project were published this year, including several proceedings papers and a presentation on automatic target detection (20) (21) (22) Jennifer Miselis published a proceedings paper using the Duck data looking at climate change implication in the area. (23)

Conclusions and Implications for Future Research

A framework has been designed to produce the MACC munitions classifier, when the relevant ground-truth data set (of munitions and non-munitions objects) is made available. An ideal test site has been chosen for the continued project: USACOE FRF at Duck, NC, has the facilities for repeated surveys of a known target field to create the signature collection needed.

Feature classifiers will then be compared using a variety of metrics, including traditional receiver operating characteristics (ROC) curves to plot probability of detection vs. probability of false alarm for a given classifier characteristic. Additionally, confusion matrices will be employed to show the skill of various feature set classifiers. We foresee the balanced success ratio for each munitions type examined as the most instructive metric to use. Balanced success ratio, $BSR = (P(success \mid +) + P(success \mid -)) / 2$, where 50% of the scoring is the percent of real targets correctly classified and 50% of the scoring is the percentage of called targets that are real targets. This is especially useful in this case where the amount of clutter objects detected will be much greater than the number of objects to detect in each munitions category.

We believe these techniques applied to parametric sonar, and magnetic detection and tested on a test range open to all will form a baseline classification capability. As improved detection sensors are deployed, this framework will document the improvements in the state of the art against a controlled test field.

References

1 SERDP; ESTCP. **Final Report SERDP and ESTCP Workshop On Technology Needs for the Charaterization, Management, and Remediation of Military Munitions in Uderwater Environments**. [S.l.]. 2007.

2 GENDRON, M.; LOHRENZ, M.; REDLINGER, L. **Method and System for Real-Time Automated Change Detection and Classification**. 2009/0016161 A1, 2009.

3 GENDRON, M.; ET AL. **The Automated Change Detection and Classification – Real-time (ACDC-RT)**. San Diego: Proceedings of The Undersea Defense Technology Symposium. 2006.

4 MISELIS, J.; MCNINCH, J. Evaluation of Interannual Changes in Nearshore Morphology and Lithology and their Relationship to Shoreline Change. **(in prep)**, 2011.

5 BIRKEMEIER, W. A. et al. **A user's guide to the Coastal Engineering Research Center's Field Research Facility**. Vicksburg, MS. 1985. (CERC-85-1).

6 LONG, C.; RESIO, D. Wind wave Spectral observations in Currituck Sound, North Carolina. **J. Geophys. Res.**, v. 9, n. 1, p. 112, 2007.

7 FENSTER, M. S.; DOLAN, R. Historical shoreline trends along the Outer Banks, NorthCarolina: Processes and responses. **Journal of Coastal Research**, v. 9, n. 1, p. 172-188, 1993.

8 US ARMY CORPS OF ENGINEERS. FRF. **US Army Corps of Engineers Field Research Facility**, 2010. Disponivel em: <http://www.frf.usace.army.mil>. Acesso em: 15 Feb 2011.

9 FARAN, J. J. Sound Scattering by solid cylinders and spheres. **J. Acoust. Soc. Am.**, v. 23, p. 405-418, 1951.

10 HACKMAN, R. H. et al. **Acoustic scattering from thin shells in bounded media and in sediments**. [S.l.]: Proc. Oceans 1989. 1989. p. 1176-1180.

11 LIM, R. et al. Scattering by objects buried in underwater sediments: Theory and experiment. **J. Acoust. Soc. Am.**, v. 93, p. 1762-1783, 1993.

12 TESEI, A. et al. Measurements and modeling of acoustic scattering from partially buried and completely buried spherical shells. **J. Acoust. Soc. Am.**, v. 112, 2002. ISSN p 1817-1830.

13 LIM, R. Acoustic scattering by a partially buried three-dimensional obstacle. **J. Acoust. Soc. Am.**, v. 104, p. 769-782, 1998.

14 STANTON, T. K. Simple approximate formulas for backscattering of sound by spherical and elongated objects. **J. Acoust. Soc. Am.**, v. 86, p. 1499-1510, 1989.

15 STANTON, T. K. Sound scattering by cylinders of finite length. II. Elastic cylinders. **J. Acoust. Soc. Am.**, v. 83, p. 64-67, 1988.

16 COHEN, L. **Time-Frequency Distributions-A Review**. Proc. of the IEEE Vol. 77, No. 7. [S.l.]: [s.n.]. 1989. p. 941-981.

17 CHOI, H. I.; WILLIAMS, W. L. Improved Time-Frequency Representation of Multicomponent Signals Using Exponential Kernels. **IEEE Trans. ASSP 37**, p. 862-871, 1989.

18 JACKSON, D. J.; RICHARDSON, M. D. **High-Frequency Seafloor Acoustics**. New York: Springer, 2007.

19 LAY, D. **Linear Algebra and Its Applications**. [S.l.]: Addison-Wesley, 2000. 441-486 p.

20 GENDRON, M.; DUBBERLEY, J.; LOHRENZ, M. **Synthetic Aperture Sonar Automatic Target Recognition Issues**. Istanbul, Turkey: Proceedings fo the 10th European Conference on Underwater Acoustics. 2010. p. 1517-1521.

21 GENDRON, M.; DUBBERLEY, J.; LOHRENZ, M. **The Science and Art of Change Detection.** Monterey, CA: Proceeding of the 9th International Symposium on Technology and the Mine Problem. 2010.

22 DUBBERLEY, J.; GENDRON, M. **Improving SAS ATR through filtering**. La Spezia, Italy: 2010 Joint Research Programme on Mine Warfare. 2010.

23 MISELIS, J. **Costal Evolution and Climate Change:** Addressing the Challenges fo Milti-scale Spatial and Temproal Variability. Buenos Aires, Argentina: IEEE/OES South America International Symposium. 2010.

Acronym List

ACDC-RT	Real-time Automated Change Detection and Classification System
ASW	Anti-Submarine Warfare
ATR	Automatic Target Recognition
AWARE	Automated Warning and Response Engine
BOSS	Buried Object Scanning Sonar
BPNN	Back-Propagation Neural Networks
BSO	Balanced Success Ratio
CASS-GRAB	Comprehensive Acoustic Simulation System / Gaussian Ray Bundle
CHIRP	Compressed High Intensity Radar Pulse
CHL	Coastal and Hydraulics Laboratory
COIN	Common Operator Interface for the Navy
CRAB	Coastal Research Amphibious Buggy
CNO	Chief of Naval Operations
CWD	Choi-Williams distribution
DoD	Department of Defense
EM	Electromagnetic
EPMA	Environmental Post-Mission Analysis
ERDC	U.S. Army Engineer Research and Development Center
ESTCP	Environmental Security Technology Certification Program
FRF	Field Research Facility (U.S. Army Corps of Engineers, Duck, NC)
GFE	Government Furnished Equipment
GUI	Graphical User Interface
IEEE	Institute of Electrical & Electronics Engineers
LARC	Light Amphibious Reconnaissance Craft
LF-SAS	Low-frequency Synthetic Aperture Sonar
MACC	3-D Munitions and Clutter Classifier
MCM	Mine Counter Measures
MEDAL	Mine Warfare. Decision Aids Library
MIW	U.S. Navy Mine Warfare
MMSON	Munitions Management Statement of Need
MTA	Marine-towed Array
NAVAIR	Naval Air Systems Command
NAVO	Naval Oceanographic Office
NOMWC	Naval Oceanography Mine Warfare Center
NRL	Naval Research Laboratory
NSF	National Science Foundation
NSWC-PCD	Naval Surface Warfare Center – Panama City Detachment
OASES	Ocean Acoustics and Seismic Exploration Synthesis
OES	Oceanic Engineering Society

ONR	Office of Naval Research
PC	Principal Component
PCA	Principal Component Analysis
PCSWAT	Personal Computer Shallow Water Acoustic Tool-Set
Pfa	Probability of False Alarms
RDT&E	Research, Development, Test, and Evaluation
REMUS	Remote Environmental Monitoring Units
ROC	Receiver Operating Characteristics
RTG	Quantum Magnetics' Realtime Tracking Gradiometer
SAIC	Science Applications International Corporation
SEED	SERDP Exploratory Development Solicitation
SERDP	Strategic Environmental Research and Development Program
SPD	Sound Pressure Level
SVM	Support Vector Machine
TCD	Target and Change Detection
TS	Target Strength
UUV	Unmanned Underwater Vehicle
UXO	Underwater Unexploded Ordinance
WVD	Wigner-Ville distribution